[*Revision 3*] Textures and high–field strength elements in hydrothermal magnetite from a skarn system: Implications for coupled dissolution–reprecipitation reactions

Shuo Yin[1], Changqian Ma[1,2]*, and Paul T. Robinson[1]

[1]School of Earth Sciences, China University of Geosciences, Wuhan, Hubei 430074, P.R. China

[2]State Key Laboratory of Geological Process and Mineral Resources, China University of Geosciences, Wuhan, Hubei 430074, P.R. China

(Shuo Yin, yinshuo1128@126.com; Changqian Ma, cqma@cug.edu.cn; Paul T. Robinson, paulrobinson94@hotmail.com.)

Abstract

There is increasing evidence to suggest that high–field strength elements (HFSE) could be mobile to some extent in hydrothermal fluid due to the influence of halogens (e.g., fluorine and chlorine). However, in natural hydrothermal (fluid) systems, “coupled dissolution reprecipitation” (CDR) reactions at fluid-mineral interfaces that have been emphasized in the past decade may play a key role in controlling the final textures and mineral assemblages. The influences of the CDR reactions in hydrothermal systems on HFSE enrichment or depletion at the mineral scale are enigmatic. In this study, we show that enrichment of Nb and Zr can occur in magnetite on the mineral scale formed by hydrothermal fluids at medium-to-lower temperature in a skarn system. Four stages of mineralization and alteration of magnetite have been identified in the Baishiya iron skarn deposit of the East Kunlun Mountains of China. Magnetite formed in stage 1 (S1) developed obvious oscillatory zonation, whereas that formed in stages 2 (S2) and 3 (S3) shows hydrothermal alteration and metasomatic textures, and that in stage 4 (S4) developed euhedral crystals with simple zoning. Systematic variations in the trace element compositions of different magnetite grains analyzed by EMPA and LA-ICP-MS suggest that the magnetite from S1 to S3 may have formed in a metasomatic process at relatively constant temperature, whereas the magnetite from S4 formed by re-equilibrium processes at lower temperature. The magnetite from each stage can be divided into light and dark domains based on back scattered electron images. The dark domains in the magnetite from S1 and S2 have higher Nb/Ta (8.52-27.00) and Zr/Hf (18.22-52.64) ratios and silicon contents than the light domains (0.55-5.66 and 2.54-16.43, respectively). Compared with other magnetite ores, that from S1 and S2 is depleted of V and Ni. This depletion may be induced by increased oxygen and co-crystallized sulfide. However, these variations are unlikely to be responsible for the enrichment of Nb and Zr in magnetite at equilibrium conditions. Conversely, the dark domains of the magnetite from S1 and S2 are porous, irregular, and/or oscillatory with quartz inclusions, indicating nonequilibrium conditions. These textural features could be attributed to the CDR reactions that are ubiquitous in skarn systems. The increased silicon concentrations in magnetite due to the CDR reactions could affect the lattice parameters of the magnetite structure, leading to an overall change in the volume of magnetite ores. The reduplicative processes of volume change, dissolution and porosity formation within magnetite are further imporved due to an incresed oxygen fugacity and co-crystallized sulfide (e.g., decreased temperature or increased sulfur fugacity) at far-from-equilibrium or local equilibrium conditions, resulting in oscillatory magnetite dark domains of S1. Ripening of the transient porosity can trap nanoscale precipitates of columbite and zircon within pores of Si-magnetite, and this precipitation could be attributed to the co-crystallized phlogopite that would incorporate fluorine from the hydrothermal fluid, and subsequently decrease the solubility of Nb and Zr in the skarn system. This scenario highlights that Nb and Zr could be scavenged and enriched into in the reaction fronts (porosity) by controlling the reaction pathway at a local scale that does not reflect the overall fluid–rock interaction history of the mineral assemblage.

Keywords: Hydrothermal magnetite, skarn deposit, high–field strength elements, coupled dissolution–reprecipitation reactions

Introduction

High–field strength elements (HFSEs) are considered as reliable geochemical indicators because of their immobility in most geological settings. However, there is increasing evidence to suggest that they are mobile to some extent in fluid-driven systems (Gao et al., 2007; Huang et al., 2012; Jiang et al., 2005; Rapp et al., 2010; Salvi and Williams-jones, 2006; Zhang et al., 2016). Recent experiments have further demonstrated that NaCl- and NaF-bearing aqueous fluids at hydrothermal conditions could improve HFSE mobility (Tanis et al., 2012; Tanis et al., 2015; Tanis et al., 2016). However, in natural hydrothermal systems, the reduplicative hydrothermal activity generally results in textural and trace element variability (Hu et al., 2015; Knipping et al. 2015a, 2015b). In the past decade, a number of studies have emphasized the role of "coupled dissolution reprecipitation reactions" (CDR) in fluid-rock interaction systems. Conditions far from equilibrium or local equilibriums at the mineral–fluid interface play a key role in controlling the final textures and mineral assemblages (Altree-Williams et al., 2015).

Skarns are ideal for the application of, rather than an exception to, self-organization theory in fluid-rock interaction systems (Ciobanu and Cook, 2004). Solid-state diffusion (SSD) in skarn minerals is retarded because the minerals generally form in hydrothermal fluids at medium-to-lower temperature (Meinert et al., 2005). Refractory skarn minerals, such as garnet, magnetite, and pyrite, can retain evidence of overprinting (Ciobanu and Cook, 2004). Recently, *in situ* textural and chemical analyses of magnetite have shown a complicated distribution of trace elements that can act as "chemical oscillators" and record metasomatic processes (Dare et al., 2014; Hu et al., 2015; Nadoll et al., 2014a).

In this study, we show that there are distinct Nb/Ta and Zr/Hf ratios and other trace elements in magnetite on mineral scale from the Baishiya iron skarn deposit of the East Kunlun orogenic belt in the northern Qinghai-Tibet Plateau. The improved mobility of HFSEs and the zonation patterns in fluid-rock reactions cannot be attributed to variations in physical and/or chemical parameters at equilibrium conditions. Based on an analysis of the textures and mineral assemblages in hydrothermal magnetite, we contend that fluid-driven coupled dissolution–reprecipitation (CDR) reactions at nonequilibrium conditions may account for these features in hydrothermal magnetite in a skarn system.

Geological setting

The East Kunlun orogenic belt (EKOB) in the northern Tibetan Plateau is a huge tectono-magmatic terrane that consists of multistage granitoid plutons (Fig. 1a) (Mo et al., 2011; Yin and Zhang, 1997). Late Paleozoic to early Mesozoic magmatic rocks are abundant in the EKOB, as evidenced by Triassic granitoids that crop out over an area of 23,000 km^2 (Fig. 1b) (Liu et al., 2004; Mo et al., 2007). The related deposits are mainly late Triassic in age and are linked with the magmatism induced by the northward subduction of the Songpan-Ganzi-Bayan Har block. The iron skarn deposits are mostly located in the contact zones of marine carbonates and late Triassic intermediate to silicic plutons. The Baishiya iron skarn deposit, located in the uplifted edge of the Dulan-Elashan belt (Fig. 1b) (Ma, 2010), is related to the granodiorite that intruded the lower members of the Dagangou Formation, which consists of limestone and dolomitic limestone (Fig. 2) (Zhang et al., 2011). The mineralized granodiorite emplaced in the Triassic was calc-alkaline and metaluminous. The eastern part of the Baishiya deposit consists of iron and zinc ore bodies, which crop out in a discontinuous mineralized contact zone approximately 2000 m long and 50-300 m wide, with a proven reserve of 8 Mt Fe at an average grade of 35–51 wt.% Fe (Fig. 2) (Zhang et al., 2011).

Petrography and textures of selected skarns

The extensive hydrothermal alteration around the Baishiya ore bodies can be divided into four stages (Fig. 3). Samples of magnetite from each of these stages were selected to show the character and composition of the magnetite produced.

In stage 1 (S1), magnetite coexisting with phlogopite and minor hedenbergite occurs as subhedral to euhedral crystals ranging from 200-500 μm in size (Fig. 4; 1a, 1b), with obvious oscillatory zoning in the back scattered electron (BSE) image (Fig. 4; 1c). Two distinct generations of magnetite formed in S1 are shown in the BSE image; light cores and darker rims can be observed in the magnetite, suggesting that the cores have lower concentrations of elements with low atomic number (less than the end-member Fe oxide). The surfaces of the dark domains are more irregular than those of the light domains, which contain minor quartz veins (Fig. 4; 1d).

Stage 2 (S2) produced vein-type magnetite that cuts across, and is intergrown with, garnet and/or hedenbergite, with some calcite within small fractures (Fig. 4; 2a, 2b). The BSE image of this magnetite shows that multistage hydrothermal alteration is recorded within the magnetite grain with well-developed porosity (Fig. 4; 2c). The light and dark domains in this magnetite are intergrown with irregular boundaries, and minor amounts of silicate minerals, including quartz, occur along the boundaries of the different generations (Fig. 4; 2d).

The ore sample formed in stage 3 (S3) consists of intergrown siderite, calcite, and magnetite (Fig. 4; 3a, 3b). The BSE images of the magnetite confirm the occurrence of multistage hydrothermal alteration characterized by two intergrown generations of the magnetite bands (Fig. 4; 3c, 3d). The light domains are relatively even and smooth, whereas the dark domains are irregular and porous, with some minor infilling of siderite. These special textures and the mineral assemblage containing abundant siderite and calcite suggest that the magnetite crystals grew in a carbonate-rich ore fluid.

The last magnetite ores, which formed during stage 4 (S4), consist mainly of massive magnetite, small amounts of subhedral to euhedral pyrite, and quartz veinlets (Fig. 4; 4a, 4b). This mineral assemblage marks the end of magnetite mineralization and the beginning of the sulfide stage, in which pyrite and sphalerite are dominant. The subhedral to euhedral magnetite crystals range in size from 50-150 μm and show distinct zoning in the SEM-BSE images. There are small cavities and minor quartz in the narrow rim of the magnetite, features that are absent in the core (Fig. 4; 4c, 4d).

Analytical methods

Polished thin sections of all samples were prepared to characterize their mineral assemblages and textural relationships. In addition, magnetite grains were separated from crushed samples and then handpicked under a binocular microscope. These grains were mounted in epoxy, polished, and carbon-coated for SEM examination and X-ray mapping. The major elements were analyzed with a JXA-8230 Superprobe at the Center for Materials Research and Analysis, Wuhan University of Technology (WUT). Standards and unknowns were analyzed with a 1-μm-diameter beam at an accelerating voltage of 20 kV and a beam current of 20 nA. The integration time was 30 s for peaks of Al, Si, and

Mg and 20 s for the remaining elements. The following standards were used: Fe_3O_4 (Fe), $Mg_3Al_2Si_3O_{12}$ (Mg, Al and Si), (Mn, Ca)SiO_3 (Ca and Mn), TiO_2 (Ti), $FeCr_2O_4$ (Cr), vanadium metal (V), and Ni_2Si (Ni).

Thirty-six elements were determined in magnetite by laser ablation-inductively coupled plasma mass spectrometry (LA-ICP-MS) using the following isotopes: ^{25}Mg, ^{27}Al, ^{29}Si, ^{31}P, ^{39}K, ^{44}Ca, ^{45}Sc, ^{49}Ti, ^{51}V, ^{53}Cr, ^{55}Mn, ^{57}Fe, ^{59}Co, ^{60}Ni, ^{65}Cu, ^{66}Zn, ^{71}Ga, ^{74}Ge, ^{85}Rb, ^{88}Sr, ^{89}Y, ^{90}Zr, ^{93}Nb, ^{95}Mo, ^{107}Ag, ^{111}Cd, ^{115}In, ^{118}Sn, ^{137}Ba, ^{178}Hf, ^{181}Ta, ^{182}W, ^{208}Pb, ^{209}Bi, ^{232}Th, and ^{238}U. Trace elements of magnetite were determined with a Coherent GeoLasPro 193-nm laser ablation system, coupled with an Agilent 7700x ICP-MS, at the State Key Laboratory of Ore Deposit Geochemistry, Institute of Geochemistry, Chinese Academy of Sciences (Gao at al., 2013). Each analysis was performed by 44-μm-diam ablating spots at 6 Hz with energy of ~100 mJ/pulse for 45 s after measuring the gas blank for 18 s. ^{57}Fe was used as an internal standard. The off-line data processing was performed using a program called ICPMSDataCal (Liu et al., 2008). USGS standard reference materials of BHVO-2G and BCR-2G were used as external standards to plot calibration curve. In order to constrain precision and accuracy of Nb, Ta, Zr and Hf, the reference material of BIR-1G with similar concentrations was used as quantity control of the time-dependent calibration for sensitivity drift, and the reference material of GSE-1G was used for other elements.

Geochemical characteristics of the Baishiya magnetite

Table 1 presents the electron microprobe compositions of the various magnetite grains. All the analyzed magnetites have relatively high SiO_2, Al_2O_3, MnO, and MgO contents. The contents of other elements, including TiO_2, Cr_2O_3, V_2O_3, CaO, and NiO, are lower or only marginally higher than their detection limits.

The magnetite grains from S1 form two compositional groups, corresponding to the dark and light domains. The dark domains have relatively high contents of SiO_2 (1.02-1.47 wt.%) and Al_2O_3 (0.93-1.66 wt.%), whereas the light domains contain significantly lesser SiO_2 (0.05-0.18 wt.%) and Al_2O_3 (0.21-0.42 wt.%). The two domains also show small differences in MgO and MnO contents, which follow the same trends as SiO_2 and Al_2O_3. The magnetite from S2 has much higher concentrations of SiO_2 in both the dark and light domains than those from S1 (1.76-4.33 wt.% and 0.58-1.13 wt.%, respectively). The contents of other elements, such as Al_2O_3, MgO, and MnO, show trend variations similar to those of SiO_2. Extremely high contents of SiO_2 occur in both the light cores and the dark rims of the magnetite from S3 (0.90-5.25 wt.%). The alumina contents range up to 0.58 wt.% in the dark domains but are mostly below detection levels in the light domains. The magnetite from S4 is strongly depleted of Al_2O_3 in both the dark and the light domains, whereas the other elements have similar concentrations to that from S3. The SiO_2 contents in the light domains of the magnetite from this sample are much lower (0.11-0.83 wt.%) compared with that from S3.

Various magnetite grains from all four mineralization stages were analyzed by LA-ICP-MS (Table 2); however, the rim of the grain from S4 was excluded because it was too narrow (10 μm) to be ablated by the laser (44 μm). In the magnetite grains of S1, although both dark domains and light domains have relatively lower concentrations (~ 0.1 to 10 ppm) of Y, Pb, Ge, W, Sc, Mo, Sn, Ga, V, Co and Ni, the Ti contents in the dark domains (10 to 100 ppm) are much lower than the light domains (100 to 1000 ppm). The dark domains of the S2 magnetite have higher contents of Sn, W and Pb (10 to 100 ppm) and lower contents of Ti (0.1 to 10 ppm) than the light domains (0.1 to 10 ppm and 10 to 100 ppm, respectively). Other elements in the magnetite of S2, such as Ge, Sc, Mo, Co, V, and Ni, range from 0.1 ppm to 10 ppm. The overall concentrations of trace elements in the magnetite from S3 are distinct higher than other magnetite grains. Lead, Ge, W, Sn, Ga, Ti, Co, V and Ni are characterized by variations in abundance (10 to 100 ppm), and Y, Sc and Mo range from 1 ppm to 10 ppm. The S4 magnetite ores have relatively constant concentrations (1 to 10 ppm) of Y, Pb, Ge, Sn, Ga, Ti, Co, V and Ni, and lower contents of Sc and Mo (0.1 to 1 ppm). In addition, the Zn concentrations in all the magnetite grains are relatively constant (100 to 500 ppm).

The magnetite from S1 shows distinct oscillatory zoning, on which significant core-to-rim increases in Si, Al, and Ca and decreases in Ti, V, and Ni are superimposed. This grain also shows variations in the Nb/Ta and Zr/Hf ratios. The dark domains have Nb contents of 5.64-11.39 ppm and Ta contents of 0.42-0.49 ppm, yielding Nb/Ta ratios of 12.59-27.00. The light domains have lower Nb (0.25-1.43 ppm) and Ta (0.13-0.44 ppm) contents, and much lower Nb/Ta ratios of 0.55-3.78. The Zr contents in the dark domains are also higher than those in the light domains (2.79-5.82 ppm and 0.36-1.29 ppm, respectively), whereas the Hf concentrations are constant (0.05-0.18 ppm and 0.10-0.28 ppm, respectively), leading to distinct Zr/Hf ratios in the dark and light domains (29.70-52.64 and 2.54-9.76, respectively). Although the magnetite grains from S1 and S2 are very different texturally, they have similar trace element contents in both their dark and light domains. The main differences are in the contents and ranges of geochemical variations of some high–field strength elements and other elements, such as Ti, V, and Ni (Table 2). The magnetite grains from S3 have relatively uniform trace element contents, although the light and dark domains contain different amounts of Si. The median concentrations of most trace elements in the magnetite from S3 are generally higher than those in other samples, especially the contents of Hf, Ta, W, Ge, Mo, and Co. The contents of Nb, Ta, Zr, and Hf are relatively constant (Nb=0.61-5.58 ppm, Ta=0.19-3.52 ppm, Zr=0.48-2.45 ppm, Hf=0.16-1.58 ppm, Nb/Ta=1.21-4.66, and Zr/Hf=1.35-7.05). The rims of the magnetite from S4 are too narrow (10 μm) to be analyzed by LA-ICP-MS; however, the microprobe analyses show that the dark domains are extremely rich in Si (up to 5 wt.%), whereas other elements, such as Ti, Al, Cr, V, and Ni, are below their detection limits. The light domains in this sample are distinctly depleted of Al, Ga, Ti, and V compared with similar domains in other samples. In addition, the variations in Nb and Ta are much lower (Nb=0.15-0.58 ppm and Ta=0.03-0.11 ppm), yielding Nb/Ta ratios of 2.03-11.65, whereas the Zr/Hf ratios have a wide range (Zr=0.87-5.08 ppm, Hf=0.05-0.10 ppm, and Zr/Hf=8.77-96.63).

Discussion

Multistage formation history of hydrothermal magnetite

The multi-element variation diagrams of magnetite developed by Dare et al. (2014) have been used (Fig. 5), aimed to readily observe anomalies in the pattern. The 25 trace elements are plotted in order of increasing compatibility into magnetite (Dare et al., 2012). Here we presented only 22 trace elements in the diagrams due to the detection limits of Cr, Cu and P. Trace elements in magnetite formed under hydrothermal process are controlled by various factors. Therefore, it is usually difficult to attribute specific element enrichment or depletion to one singular physicochemical factor (Nadoll et al., 2014a). To probe into these factors (e.g., temperature, oxygen and sulfur fugacities) from S1 to S4, the magnetite trace elements patterns of high and low temperature hydrothermal systems, andesite and I-type granite compiled by Dare et al. (2014) have been taken into comparison.

Temperature. The magnetite ores are characteristic with a gradual decrease of V and Ti contents, and a slight increase in Al and Mn contents (Fig. 6a), indicating a typical evolution trend of a skarn system (Dare et al., 2014; Dupuis and Beaudoin, 2011; Nadoll et al., 2014b). However, the sample from S4, which has extremely low contents of Ti and V, may have formed at a lower temperature compared with the others. This possibility is supported by the low contents of Ga in this sample (Fig. 6b) because Ga concentrations are believed to correlate positively with temperature (Nadoll et al., 2014a). Nadoll et al. (2014a) considered that foreign cations in hydrothermal magnetite can be continuously expelled by re-equilibration, as has been shown by a study of different iron skarn deposits (Hu et al., 2015). A strong depletion of Si, Al, V, and Ti, leading to a higher mass fraction of Fe at lower temperature, suggests that the magnetite from S4 was re-equilibrated during cooling (Fig. 6c). Although we cannot calculate the temperature of each stage, all of these features indicate that the magnetite ores from S4 are indeed distinct from other samples from S1 to S3.

Sulfur fugacity. Lead and W are considered to be relatively incompatible into magnetite (Dare et al., 2014). Their concentrations in hydrothermal fluid may increase gradually as magnetite crystallizes from the fluid. This, in turn, will result in higher contents of these two elements in magnetite. In the multi-element variation diagrams, compared with other hydrothermal magnetites, the anomalies of Pb and W can be observed (Fig. 5), and they increased by several orders of magnitude from S1 to S3 (Fig. 6d). However, in the magnetite ores of S4, their concentrations decreased sharply. Based on our field work and petrography (Fig. 3), we suggest that the competition of galena and scheelite for Pb and W in the hydrothermal fluid of S4 respectively, could account for this scenario (Fig. 6d). In addition, the occurrence of pyrite in magnetite ores of S4 (Fig. 4; 4a) further confirmed that the hydrothermal fluid in this stage allowed sulfide to precipitate. In a skarn system, the transition from magnetite to sulfide could be driven by either decreased temperature or increased sulfur fugacity. If the temperature of S4 decreased, as the discussion above, the sulfur fugacity may be constant.

Oxygen fugacity. Magnetites with high contents of silicon ($SiO_2 > 1\%$) are called silician magnetites (Shimazaki, 1998). These have been found in banded iron formations, serpentinite, skarn deposits, and volcanic rocks that formed over low-to-high temperatures (Huberty et al., 2012; Newberry et al., 1982; Shcheka et al., 1977; Westendorp et al., 1991). A recent study also showed that Si can be incorporated in the tetrahedral site of magnetite (Xu et al., 2014). Thus, in the present work, the dark domains in the magnetite from S1 and S2 could have been promoted by high concentrations of aqueous silica and Fe-carbonate complex species in pore fluid during the metasomatic process (DolejŠ and Manning, 2010; Xu et al., 2014), as evidenced by the enclosed quartz (Fig. 4; 1d,2d) and siderite (Fig. 4; 3a,3b). However, compared with other magnetite ores, these dark domains have lower contents of V and Ni (Fig. 5). The vanadium concentration in magnetite is a function of temperature and oxygen fugacity (Toplis and Corgne, 2002), whereas the Ni content is sensitive to co-crystallizing sulfide phases due to their competition for Ni in the ore-bearing fluid (Dare et al., 2012). If this was the scenario for the depletion, regardless of the fluid composition, the trigger could be an increased oxygen fugacity and co-crystallized sulfide phases in a typical skarn deposit. Huberty et al. (2012) reported the overgrowth of silician magnetite (1 to 3 wt.% SiO_2) from the Dales Gorge banded iron formation (Western Australia); the pure magnetite domains are porous with numerous mineral inclusions, whereas the silician magnetite domains are relatively smooth and devoid of mineral inclusions. They suggested that the reducing conditions are necessary to stabilize silician magnetite.

However, in our case, the silician magnetites from S1 and S2 are porous, irregular, and/or oscillatory with quartz inclusions (Fig. 4; 1d, 2d), which are contrary to magnetite from Dales Gorge. Based on their conclusion, we consider that the part dissolution of silician magnetites from S1 and S2 may be explained by an increased oxygen fugacity.

Mobility of high–field strength elements in hydrothermal fluid

There are wide ranges of high–field strength elements in magnetite on the mineral scale. The magnetite dark domains of S1 and S2 displayed distinct higher ratios of Nb/Ta and Zr/Hf than the light domains (Fig. 7), and these two ratios correlate positively with the V and Ni contents. As previously discussed, the dark domains in the magnetites from S1 and S2 may form with an increased oxygen fugacity and simultaneously precipitated sulfide. Although experiments have demonstrated that oxygen fugacity is linked with Nb-Ta fractionation, it occurred only during planetary accretion and core formation with extremely reducing conditions (Cartier et al., 2014). Therefore, variation of these conditions cannot account for the enrichment of Zr and Nb, and other factors should be taken into consideration.

Mineral inclusions. The well-developed porosity in the dark domains with higher Nb/Ta and Zr/Hf ratios suggests that the influence of the mineral inclusions in magnetite is inevitable. The electron microprobe (EMPA) analyses indicate that magnetite ores from the Baishiya deposit have high concentrations of Si, Al, and Mn, which are nominally incompatible in magnetite, and that these concentrations are higher than the contents of compatible elements, such as Ni, V, Cr, and Ti. The mineral inclusions in magnetite, if any, are more likely to be quartz, siderite, and aluminum silicate, which are enriched in Si, Al, and Mn, respectively. The comparison between the LA-ICP-MS and the EMPA analyses of Si, Al, and Mn in magnetite further confirms the involvement of these mineral inclusions in some magnetite ores (Fig. 8b). On this basis, we suggest that quartz inclusions in magnetite may have occurred in S1 (light domains), S3, and S4, whereas siderite inclusions were presumably enclosed in the magnetite during S1 (light domains) and S4. The aluminum silicate inclusions may appear only in S2 (light domains) (Fig. 8b). It is worth noting that these inclusions are not enclosed in the dark domains of the magnetites from S1 and S2 (Fig. 8a), which have higher Nb/Ta and Zr/Hf ratios than the light domains (Fig. 7). Therefore, the mineral inclusions at the micron scale in magnetite are not responsible for the enrichment of Nb and Zr. However, if columbite and zircon are incorporated in magnetite at the submicron or nanoscale, they cannot be detected by LA-ICP-MS (Fig. 9).

Fluid chemistry. The magmatic-hydrothermal evolution process in a skarn system generally has more than one pulse of hydrothermal activity. If some hydrothermal activities are originated from the 'external' magmas, the variation of fluid chemistry may also result in the enrichment of Nb and Zr on the mineral scale. In the multi-element variation diagrams of magnetite developed by Dare et al. (2014), the Nb/Ta and Zr/Hf ratios in magmatic magnetites correlate positively with their Ti, V, and Ni concentrations, which are distinct from this study (Fig. 5a, b). If skarns in this case have not been disturbed by the 'external' magmas, they are ideal for application of self-organization theory in fluid-rock interaction systems (Ciobanu and Cook, 2004); the fluid chemistry changed progressively from S1 to S4 due to the co-crystallizing minerals. In the Baishiya deposit, minerals enriched in Nb, Ta, Zr, and Hf, such as columbite-tantalite, zircon, and rutile, are invisible in field investigation, microscope observation, and BSE images, indicating that the influence of co-crystallizing mineral phases may not be dominant.

The CDR reactions. The porous, irregular, and/or oscillatory magnetite dark domains from S1 and S2 with an increased oxygen fugacity and simultaneously precipitated sulfide suggested that they are presumably far from equilibrium or at local equilibrium conditions. In terms of nonequilibrium conditions, two possibilities may account for the different mobilities of HFSEs on the mineral scale. Solid-state diffusion (SSD) has been shown to be responsible for the kinetic fractionation of Nb and Ta based on their diffusivities (Marschall et al., 2013). However, SSD could be dominant mainly at high temperature, such as magmatic processes, in which atomic diffusion within crystals overcomes activation energy barriers (Altree-Williams et al., 2015). Alternatively, in hydrothermal fluid, the CDR reactions could provide a kinetically more favorable pathway (Putnis, 2002; Zhao et al., 2013), which has been emphasized in the past decade (Altree-Williams et al., 2015; Arai and Akizawa, 2014; Harlov et al., 2011; Putnis, 2009; Putnis and Austrheim, 2010; Ruiz-Agudo et al., 2014). The well-developed porosity in the dark domains of the magnetites from S1 and S2 is influenced by an overall change in volume during the CDR reactions in a porous fluid-flow system. This volume change could be attributed to the variation in Si concentrations in the magnetite structure because the derived lattice parameters of silician magnetite have changed compared with pure magnetite (Huberty et al., 2012). In addition, combining Z-contrast imaging and ab initio calculation using density functional theory (DFT) method, Xu et al. (2014) confirmed that the Si-magnetite nano-precipitates distribute along {111} of the host magnetite. These characteristics suggest that Nb and Zr may also be incorporated in nanoscale precipitates (e.g., columbite and zircon), and thus enriched in the ubiquitous porosity of the host silician magnetite. The reason for the existence of nanoscale mineral inclusions is that the partition coefficients for Nb and Zr correlate positively with Ti concentrations and temperature, but negatively with Al concentrations (Nielsen and Beard, 2000). The enrichment of Nb and Zr in the dark domains of magnetite are characterized by sharp decrease of Ti contents, but increase of Al and Si contents (Fig. 10), which are completely opposite with the solid solution.

Chlorine and fluorine. If the porous magnetite dark domains could capture the nanoscale precipitates, that means the solubility of Nb and Zr in hydrothermal fluid decreased. The cause of this decrease is likely to be related to the decreased fluorine concentrations in hydrothermal fluid. In the alkaline magmatic systems with high contents of fluoride, Zr and Nb could be hydrothermally transported (e.g., (Zr, Nb)-fluoride) to form related Zr–REE–Nb ore deposits (Salvi and Williams-jones, 2006; Yang et al., 2013). Recent experiments have further demonstrated that chloride and fluoride-bearing aqueous fluids at hydrothermal conditions could remarkably improve

HFSE solubility (e.g., 20 wt% NaCl or 2 wt% NaF) (Tanis et al., 2015; Tanis et al., 2016). These contents of chlorine and fluorine in hydrothermal fluid are comparable to a skarn system associated with calc-alkaline granodiorite, such as the Baisihya iron skarn deposit. In the magnetite ores, the occurrence of phlogopite (Fig. 1b), as a ubiquitous crystallized mineral phase, could account for the decrease of fluorine concentrations due to its high compatibility into phlogopite (Icenhower and London, 1997; Loferski and Ayuso, 1995). If the hydrothermal fluid becomes depleted in fluorine, nanoscale precipitates such as columbite and zircon, would occur, and subsequently be adsorbed by the porous magnetite dark domains in the CDR reactions at nonequilibrium conditions.

Implications for the CDR reactions

The fluid-rock interactions span a very wide range of possible reactions, and are responsible for most of the mineral assemblages in the shallow crust (Putnis, 2009). Even in the deep subduction zone at high teperature (>900 °C), redistribution of slowly diffusing trace elements in the presence of fluid could also be recorded (Ague and Axler, 2016). The role of the CDR reactions in a number of recent studies has been emphasized for the textural and compositional complexities of minerals in these fluid-driven reactions (Arai and Akizawa, 2014; Broom-Fendley et al., 2016; Harlov et al., 2011; Li et al., 2015; Ruiz-Agudo et al., 2014; Schwartz et al., 2010; Tooth et al., 2011).

Textural observations are crucial for deciphering the origin and geological history of rocks and their constituting minerals in the CDR reactions (Altree-Williams et al., 2015).

The well-developed porosity at the mineral-fluid interface is generally promoted by a corresponding volume change, and necessary for the propagation of further dissolution within the mineral (Putnis, 2015). A similar process in the magnetite dark domains of S1 and S2 could be attributed to the silicon substitution in the magnetite structure, resulting in the intergrowth of nanoscale Si-magnetite and pure magnetite (Xu et al., 2014). The reduplicative processes of volume change, dissolution and porosity formation within magnetite are further improved due to an increased oxygen fugacity and co-crystallized sulfide (e.g., decreased temperature or increased sulfur fugacity) at far-from-equilibrium or local equilibrium conditions, which is consistent with the porous, irregular, and/or oscillatory magnetite dark domains.

At the mineral-fluid interface of the CDR reactions, these local equilibrium conditions (e.g., sulfidation, reduction) could be established pervasively. Trace and minor elements could be scavenged in the reaction fronts by controlling the reaction pathway at a local scale that does not reflect the overall fluid–rock interaction history of the mineral assemblage (Altree-Williams et al., 2015). Hydrothermal experiment on Bi–Au melts showed that the replacement of pyrrhotite by magnetite under favorably local geochemical conditions (e.g., reduced, low $a\mathrm{H_2S}$, and catalytic surface) could promote the formation of high transient porosity (Tooth et al., 2011). At the reaction front, Tooth et al. (2011) have discovered maldonite inclusions (≤2 μm) and Bi blebs in the porous magnetite, indicating that the Bi-melts could continue scavenging Au from the hydrothermal fluids passing through the CDR reactions. The key role of the CDR reactions in scavenging U during the experimental sulfidation of hematite to chalcopyrite under hydrothermal conditions has also been identified (Li et al., 2015). In this experiment, a thin U-rich line that consists of nanocrystals marked the original hematite grain surface by changing the reaction pathway. In our research, the Nb and Zr endowment in the magnetite dark domains of S1 and S2, are likely to be composed of nanoscale precipitates of columbite and zircon that formed at reaction front of nano Si-magnetite and pure magnetite. Reduplicative CDR reactions at local equilibrium conditions resulted in oscillatory magnetite dark domains of S1, and ripening of the transient porosity can trap these nanocrystals within pores of Si-magnetite. These magnetite dark domains may be further altered by late hydrothermal fluid to form the S2 magnetite dark domains.

The precipitation of nanoscale columbite and zircon, could result from the decreased solubility of Nb and Zr presumably triggered by the decreased fluorine concentrations because these elements would be hydrothermally transported (Tanis et al., 2015; Tanis et al., 2016). This influence of fluorine has also been identified in the alkaline magmatic systems with high contents of fluoride and Zr–REE–Nb ore deposits (Salvi and Williams-jones, 2006; Yang et al., 2013). Recent studies on the CDR reactions have further confirmed that halogens (e.g., chlorine and fluorine) are crucial to preferential transport of Cr and light-rare-earth-elements (Arai and Akizawa, 2014; Broom-Fendley et al., 2016). In the magnetite ores of the Baishiya deposit, the decrease of fluorine concentrations in the hydrothermal fluid could be caused by the crystallization of phlogopite due to the high compatibility of fluorine into phlogopite (Icenhower and London, 1997; Loferski and Ayuso, 1995). The similar scenario also occurred in the dehydration process that transformed blueschist into eclogite, western Tianshan, China. Precipitation of F-bearing apatite depleted the fluorine concentrations in the fluid, resulting in the decreased solubility of Ti, Nb, and Ta and the formation of hydrothermal rutile crystals (Gao et al., 2007).

Acknowledgements

We thank Fuhao Xiong and Yuheng Guo for their assistance in the field and in the sample preparation; Junmei Yang and Xiaoqian Nie for their help in the microprobe analyses; Zhihui Dai for his assistance in the LA-ICP-MS analyses; and Jianwei Li and Yuanbao Wu for their helpful discussion. This research was supported by the National Science Foundation of China (grant 41272079), the National Basic Research Program of China (grant 2012CB416802) and the National Science Foundation of China (grant 41572048).

References Cited

Ague, J.J., and Axler, J.A. (2016) Interface coupled dissolution-reprecipitation in garnet from subducted granulites and ultrahigh-pressure rocks revealed by phosphorous, sodium, and titanium zonation. American Mineralogist, 101, 1696-1699.

Altree-Williams, A., Pring, A., Ngothai, Y., and Brugger, J. (2015) Textural and compositional complexities resulting from coupled dissolution–reprecipitation reactions in geomaterials. Earth-Science Reviews, 150, 628-651.

Arai, S., and Akizawa, N. (2014) Precipitation and dissolution of chromite by hydrothermal solutions in the Oman ophiolite: New behavior of Cr and chromite. American Mineralogist, 99, 28-34.

Broom-Fendley, S., Styles, M.T., Appleton, J.D., Gunn, G., and Wall, F. (2016) Evidence for dissolution-reprecipitation of apatite and preferential LREE mobility in carbonatite-derived late-stage hydrothermal processes. American Mineralogist, 101, 596-611.

Cartier, C., Hammouda, T., Boyet, M., Bouhifd, M.A., and Devidal, J.-L. (2014) Redox control of the fractionation of niobium and tantalum during planetary accretion and core formation. Nature Geoscience, 7, 573-576.

Ciobanu, C.L., and Cook, N.J. (2004) Skarn textures and a case study: the Ocna de Fier-Dognecea orefield, Banat, Romania. Ore Geology Reviews, 24, 315-370.

Dare, S.A.S., Barnes, S.-J., and Beaudoin, G. (2012) Variation in trace element content of magnetite crystallized from a fractionating sulfide liquid, Sudbury, Canada: Implications for provenance discrimination. Geochimica et Cosmochimica Acta, 88, 27-50.

Dare, S.A.S., Barnes, S.-J., Beaudoin, G., Méric, J., Boutroy, E., and Potvin-Doucet, C. (2014) Trace elements in magnetite as petrogenetic indicators. Mineralium Deposita, 49, 785-796.

Dupuis, C., and Beaudoin, G. (2011) Discriminant diagrams for iron oxide trace element fingerprinting of mineral deposit types. Mineralium Deposita, 46, 319-335.

DolejŠ, D., and Manning, C.E. (2010) Thermodynamic model for mineral solubility in aqueous fluids: theory, calibration and application to model fluid-flow systems. Geofluids. 10, 20-40.

Gao, J.F., Zhou, M.F., Lightfoot, P.C., Wang, C.Y., Sun, M., and Qi, L. (2013) Sulfide Saturation and Magma Emplacement in the Formation of the Permian Huangshandong Ni-Cu Sulfide Deposit, Xinjiang, Northwestern China. Economic Geology, 108, 1833-1848.

Gao, J., John, T., Klemd, R., and Xiong, X. (2007) Mobilization of Ti–Nb–Ta during subduction: Evidence from rutile-bearing dehydration segregations and veins hosted in eclogite, Tianshan, NW China. Geochimica et Cosmochimica Acta, 71, 4974-4996.

Harlov, D.E., Wirth, R., and Hetherington, C.J. (2011) Fluid-mediated partial alteration in monazite: the role of coupled dissolution–reprecipitation in element redistribution and mass transfer. Contributions to Mineralogy and Petrology, 162, 329-348.

Hu, H., Lentz, D., Li, J.-W., McCarron, T., Zhao, X.-F., and Hall, D. (2015) Reequilibration processes in magnetite from iron skarn deposits. Economic Geology, 110, 1-8.

Huang, J., Xiao, Y., Gao, Y., Hou, Z., and Wu, W. (2012) Nb-Ta fractionation induced by fluid-rock interaction in subduction-zones: constraints from UHP eclogite- and vein-hosted rutile from the Dabie orogen, Central-Eastern China. Journal of Metamorphic Geology, 30, 821-842.

Huberty, J.M., Konishi, H., Heck, P.R., Fournelle, J.H., Valley, J.W., and Xu, H. (2012) Silician magnetite from the Dales Gorge Member of the Brockman Iron Formation, Hamersley Group, Western Australia. American Mineralogist, 97, 26-37.

Icenhower, J.P., and London, D. (1997) Partitioning of fluorine and chlorine between biotite and granitic melt: experimental calibration at 200 MPa H2O. Contributions to Mineralogy & Petrology, 127, 17-29.

Jiang, S.-Y., Wang, R.-C., Xu, X.-S., and Zhao, K.-D. (2005) Mobility of high field strength elements (HFSE) in magmatic-, metamorphic-, and submarine-hydrothermal systems. Physics and Chemistry of the Earth, Parts A/B/C, 30, 1020-1029.

Knipping, J.L., Bilenker, L.D., Simon, A.C., Reich, M., Barra, F., Deditius, A.P., Lundstrom, C., Bindeman, I., and Munizaga, R. (2015a) Giant Kiruna-type deposits form by efficient flotation of magmatic magnetite suspensions. Geology, 43, 591-594.

Knipping, J.L., Bilenker, L.D., Simon, A.C., Reich, M., Barra, F., Deditius, A.P., Wälle, M., Heinrich, C.A., Holtz, F., and Munizaga, R. (2015b) Trace elements in magnetite from massive iron oxide-apatite deposits indicate a combined formation by igneous and magmatic-hydrothermal processes. Geochimica et Cosmochimica Acta, 171, 15-38.

Li, K., Pring, A., Etschmann, B., Macmillan, E., Ngothai, Y., O'Neill, B., Hooker, A., Mosselmans, F., and Brugger, J. (2015) Uranium scavenging during mineral replacement reactions. American Mineralogist, 100, 1728-1735.

Liu, C., Mo, X., Luo, Z., Yu, X., Chen, H., Li, S., and Zhao, X. (2004) Mixing events between the crust- and mantle-derived magmas in Eastern Kunlun: evidence from zircon SHRIMP II chronology. Chinese Science Bulletin, 49, 828-834.

Liu, Y., Hu, Z., Gao, S., Gunther, D., Xu, J., Gao, C., and Chen, H. (2008) In situ analysis of major and trace elements of anhydrous minerals by LA-ICP-MS without applying an internal standard. Chemical Geology, 257, 34-43.

Loferski, P.J., and Ayuso, R.A. (1995) Petrography and mineral chemistry of the composite Deboullie pluton, northern Maine, U.S.A.: Implications for the genesis of Cu-Mo mineralization. Chemical Geology, 123, 89-105.

Ma, H.Y. (2010) Metallotectonics and Geochemistry of Baishiya Iron-Polymetallic Deposit, Dulan, Qinhai, China. Master's thesis, Central South University, Changsha.

Marschall, H.R., Dohmen, R., and Ludwig, T. (2013) Diffusion-induced fractionation of niobium and tantalum during continental crust formation. Earth and Planetary Science Letters, 375, 361-371.

Meng, F., Cui, M., Wu, X., and Ren, Y. (2015) Heishan mafic–ultramafic rocks in the Qimantag area of Eastern Kunlun, NW China: Remnants of an early Paleozoic incipient island arc. Gondwana Research, 27, 745-759.

Meinert, L., Dipple, G., and Nicolescu, S. (2005) World skarn deposits. Economic

Geology, 100, 299-336.

Mo, X.X., Luo, Z.H., Deng, J.F., Yu, H.D., Liu, C.D., Shen, H.W., Yuan, W.M., and Liu, Y.H. (2007) Granitoids and Crust Growth in East-Kunlun Orogenic Belt. Geological Journal of China Universities, 13, 403-414.

Mo, X.X., Luo, Z.H., Deng, J.F., Yu, X.H., Liu, C.D., Yuan, W., and Bi, X. (2011) Granitoids and crustal growth in the East-Kunlun orogenic belt. AGU Fall Meeting Abstracts, 1, p. 2370.

Nadoll, P., Angerer, T., Mauk, J.L., French, D., and Walshe, J. (2014a) The chemistry of hydrothermal magnetite: A review. Ore Geology Reviews, 61, 1-32.

Nadoll, P., Mauk, J.L., Leveille, R.A., and Koenig, A.E. (2014b) Geochemistry of magnetite from porphyry Cu and skarn deposits in the southwestern United States. Mineralium Deposita, 50, 493-515.

Newberry, N.G., Peacor, D.R., Essene, E.J., and Geissman, J.W. (1982) Silicon in magnetite: High resolution microanalysis of magnetite-ilmenite intergrowths. Contributions to Mineralogy and Petrology, 80, 334-340.

Nielsen, R.L., and Beard, J.S. (2000) Magnetite–melt HFSE partitioning. Chemical Geology, 164, 21-34.

Putnis, A. (2002) Mineral replacement reactions: from macroscopic observations to microscopic mechanisms. Mineralogical Magazine, 66, 689-708.

Putnis, A. (2009) Mineral Replacement Reactions. Reviews in Mineralogy and Geochemistry, 70, 87-124.

Putnis, A., and Austrheim, H. (2010) Fluid-induced processes: metasomatism and metamorphism. Geofluids, 10, 254-269.

Putnis, A. (2015) Transient Porosity Resulting from Fluid–Mineral Interaction and its Consequences. Reviews in Mineralogy and Geochemistry, 80, 1-23.

Rapp, J.F., Klemme, S., Butler, I.B., and Harley, S.L. (2010) Extremely high solubility of rutile in chloride and fluoride-bearing metamorphic fluids: An experimental investigation. Geology, 38, 323-326.

Rudnick, R., and Gao, S. (2003) Composition of the continental crust. Treatise on geochemistry, 3, 1-64.

Ruiz-Agudo, E., Putnis, C.V., and Putnis, A. (2014) Coupled dissolution and precipitation at mineral–fluid interfaces. Chemical Geology, 383, 132-146.

Salvi, S., and Williams-jones, A. (2006) Alteration, HFSE mineralisation and hydrocarbon formation in peralkaline igneous systems: Insights from the Strange Lake Pluton, Canada. Lithos, 91, 19-34.

Schwartz, J.J., John, B.E., Cheadle, M.J., Wooden, J.L., Mazdab, F., Swapp, S., and Grimes, C.B. (2010) Dissolution–reprecipitation of igneous zircon in mid-ocean ridge gabbro, Atlantis Bank, Southwest Indian Ridge. Chemical Geology, 274, 68-81.

Shcheka, S., Romanenko, I., Chubarov, V., and Kurentsova, N. (1977) Silica-bearing magnetites. Contributions to Mineralogy and Petrology, 63, 103-111.

Shimazaki, H. (1998) On the occurrence of silician magnetites. Resource Geology, 48, 23-29.

Tanis, E.A., Simon, A., Tschauner, O., Chow, P., Xiao, Y., Shen, G., Hanchar, J.M., and Frank, M. (2012) Solubility of xenotime in a 2 M HCl aqueous fluid from 1.2 to 2.6 GPa and 300 to 500 C. American Mineralogist, 97, 1708-1713.

Tanis, E.A., Simon, A., Tschauner, O., Chow, P., Xiao, Y., Burnley, P., Cline, C.J., Hanchar, J.M., Pettke, T., Shen, G., and Zhao, Y. (2015) The mobility of Nb in rutile-saturated NaCl- and NaF-bearing aqueous fluids from 1–6.5 GPa and 300–800 °C. American Mineralogist, 100, 1600-1609.

Tanis, E.A., Simon, A., Zhang, Y., Chow, P., Xiao, Y., Hanchar, J.M., Tschauner, O., and Shen, G. (2016) Rutile solubility in NaF–NaCl–KCl-bearing aqueous fluids at 0.5–2.79GPa and 250–650°C. Geochimica et Cosmochimica Acta, 177, 170-181.

Tooth, B., Ciobanu, C.L., Green, L., O'Neill, B., and Brugger, J. (2011) Bi-melt formation and gold scavenging from hydrothermal fluids: An experimental study. Geochimica et Cosmochimica Acta, 75, 5423-5443.

Toplis, M.J., and Corgne, A. (2002) An experimental study of element partitioning between magnetite, clinopyroxene and iron-bearing silicate liquids with particular emphasis on vanadium. Contributions to Mineralogy and Petrology, 144, 22-37.

Westendorp, R.W., Watkinson, D.H., and Jonasson, I.R. (1991) Silicon-bearing zoned magnetite crystals and the evolution of hydrothermal fluids at the Ansil Cu-Zn mine, Rouyn-Noranda, Quebec. Economic Geology, 86, 1110-1114.

Xu, H., Shen, Z., and Konishi, H. (2014) Si-magnetite nano-precipitates in silician magnetite from banded iron formation: Z-contrast imaging and ab initio study. American Mineralogist, 99, 2196-2202.

Yang, W.-B., Niu, H.-C., Shan, Q., Sun, W.-D., Zhang, H., Li, N.-B., Jiang, Y.-H., and Yu, X.-Y. (2013) Geochemistry of magmatic and hydrothermal zircon from the highly evolved Baerzhe alkaline granite: implications for Zr–REE–Nb mineralization. Mineralium Deposita, 49, 451-470.

Yin, H.F., and Zhang, K.X. (1997) Characteristics of the eastern Kunlun orogenic belt. Earth Science—Journal of China University of Geosciences, 22, 339-342.

Zhang, F.Y., Cai, Y.P., Liu, J.H., Cui, Z.Y., Li, Y.N., Ye, Y.J., Wang, Y., and Jia, S.Q. (2011) Geological Characteristics and Prospecting Indications of Baishiya Iron Deposit, Qinghai Province. Gold Science and Technology, 19, 49-54.

Zhang, L., Zhang, L., Lü, Z., Bader, T., and Chen, Z. (2016) Nb–Ta mobility and fractionation during exhumation of UHP eclogite from southwestern Tianshan, China. Journal of Asian Earth Sciences, 122, 136-157.

Zhao, J., Brugger, J., Xia, F., Ngothai, Y., Chen, G., and Pring, A. (2013) Dissolution-reprecipitation vs. solid-state diffusion: Mechanism of mineral transformations in sylvanite, $(AuAg)_2Te_4$, under hydrothermal conditions. American Mineralogist, 98, 19-32.

Figure captions

Figure 1. (a) Tectonic outline of the Tibetan Plateau showing the location of the East

Kunlun orogenic belt and (b) simplified geological map of the East Kunlun metallogenic belt (modified from Meng et al., 2015).

Figure 2. Geological map of the Baishiya iron skarn deposits (modified from Zhang et al., 2011).

Figure 3. Paragenetic sequence of alteration and mineralization at the Baishiya iron skarn deposit.

Figure 4. Hand specimens, photomicrographs, backscattered electron (BSE) images, and silicon map of magnetite formed in four stages (S1, S2, S3, and S4) of mineralization in the Baishiya iron skarn deposit. S1: euhedral-granular magnetite with phlogopite and hedenbergite; S2: vein-type magnetite cutting garnet with some calcite in small fractures; S3: banded magnetite intergrown with siderite and calcite; and S4: massive magnetite with pyrite and quartz. Note that some minerals (e.g., pyrite and calcite) may not be visible in the thin sections. In S1, two generations of magnetite are distinguished by dark and light domains; the dark domains show distinctive oscillatory zoning. Red indicates quartz. In S2, the magnetite also shows multiple generations, with minor quartz in the boundary between generations. In S3, two generations of magnetite are shown, both with high silica contents separated by zones of siderite (black). In S4, a narrow rim in a magnetite grain with high silica content and minor quartz (red to yellow) is shown. Phl,

phlogopite; Grt, garnet; Sid, siderite; Mag, magnetite; Cal, calcite; Q, quartz; Hed, hedenbergite.

Figure 5. LA-ICP-MS results of magnetite grains from stage 1 (a), stage 2 (b), stage 3 (c) and stage 4 (d) of Baishiya are normalized to bulk continental crust (Rudnick and Gao, 2003). Results of this study are compared to magnetite trace elements patterns of high and low temperature hydrothermal systems, andesite and I-type granite defined by Dare et al. (2014).

Figure 6. (a) Diagram of V+Ti versus Al+Mn in hydrothermal magnetite from the Baishiya deposit, based on Nadoll et al. (2014b). (b) Diagram of gallium versus Sn in magnetite from the Baishiya deposit and other localities, modified from Nadoll et al. (2014a). Lower concentrations of Ga and Sn are suggested to be linked to lower temperatures. The concentrations of gallium, in particular, are significant in magnetite formed at low temperatures (Nadoll et al., 2014a). The Ga contents of sample DL14-14 are distinct from those of other samples, indicating a lower formation temperature. (c) Diagram of gallium versus Fe (wt.%). The grade of ore samples formed by metasomatic processes is variable, whereas that of sample DL14-14 is high and relatively uniform, indicating late re-equilibration. (d) Diagram of Pb versus W in magnetite ores of Baishiya. The Pb contents correlate positively with W contents. Note that the concentrations of P and W increased from stage 1 to stage 3, but decreased sharply in stage 4, indicating

co-crystallized minerals of galena and scheelite.

Figure 7. Multiple plots of hydrothermal magnetite from the Baishiya iron skarn deposit. (a) Nb/Ta ratios versus V contents, (b) Nb/Ta ratios versus Ni contents, (c) Zr/Hf ratios versus V contents, and (d) Zr/Hf ratios versus Ni contents.

Figure 8. LA-ICP-MS and electron microprobe (EMPA) analyses of the Si, Al, and Mn contents (average values) of Baishiya magnetite from stages 1 (S1) to 4 (S4). (a) The Si, Al, and Mn contents of magnetite as analyzed by LA-ICP-MS are in good agreement with the EMPA analysis results for most samples. Note that all these elements analyzed by LA-ICP-MS and EMPA from dark domains of S1 and S2 are matched with each other. (b) The contents of Si in magnetite from S1 (light domains), S3, and S4 and of Mn in magnetite from S1 (light domains) and S4 are slightly higher in the LA-ICP-MS than in the EMPA analysis, indicating that quartz and siderite (enriched in Mn) inclusions may be involved. Only the magnetite from S1 (light domains) has slightly higher concentrations of Al in the LA-ICP-MS than in the EMPA analysis, suggesting that inclusions of aluminum silicate minerals are not dominant in the magnetite ores.

Figure 9. Time-resolved analytical signals of represented LA-ICP-MS analyses. Mineral inclusions in magnetite ores of Baishiya deposit are mainly composed of siderite, quartz and aluminum silicate that could account for the abnormal elements such as Mn, Si and

Sample	DL15-3 (wt.%) (dark)						DL15-3 (wt.%) (light)						
No.	1	2	3	4	5	6	1	2	3	4	5	6	7
SiO_2	1.47	1.20	1.02	1.09	1.18	1.18	0.12	0.17	0.05	0.18	0.06	0.11	0.10
TiO_2	0.00	0.05	0.00	0.00	0.00	0.00	0.20	0.20	0.13	0.22	0.07	0.07	0.00

Al.

Figure 10. Elemental maps of magnetite ores from stage 1 in the Baishiya deposit. Sharp reaction fronts between the Si-magnetite and relatively pure magnetite have formed the oscillatory zonation in the rim of the magnetite grain (S1), indicating the coupled dissolution–reprecipitation reactions at nonequilibrium conditions.

Al_2O_3	1.66	1.47	0.93	1.42	1.04	1.04	0.21	0.42	0.23	0.32	0.24	0.33	0.22
Cr_2O_3	0.00	0.00	0.00	0.00	0.01	0.01	0.00	0.00	0.00	0.00	0.00	0.01	0.01
V_2O_3	0.01	0.00	0.01	0.00	0.01	0.01	0.01	0.00	0.01	0.01	0.00	0.00	0.01
FeO	87.94	88.69	90.06	88.65	89.52	89.52	90.59	91.14	91.34	91.49	91.00	91.66	91.80
MnO	0.21	0.15	0.11	0.21	0.14	0.14	0.11	0.18	0.06	0.14	0.07	0.06	0.05
MgO	0.65	0.53	0.35	0.50	0.37	0.37	0.20	0.19	0.29	0.23	0.28	0.23	0.19
CaO	0.26	0.25	0.12	0.19	0.15	0.15	0.00	0.00	0.00	0.00	0.00	0.00	0.00
NiO	0.00	0.01	0.00	0.00	0.00	0.00	0.00	0.00	0.00	0.00	0.00	0.00	0.00
Total	92.21	92.35	92.60	92.07	92.42	92.42	91.44	92.31	92.11	92.59	91.72	92.48	92.38

Table 1 Summary of EMPA results for major elements in magnetite from Baishiya deposit

Sample	DL2#01 (wt.%) (dark)							DL2#01 (wt.%) (light)					
No.	1	2	3	4	5	6	7	8	9	11	12	13	14
SiO_2	3.01	1.76	2.84	3.53	4.12	4.14	4.33	1.01	1.13	0.91	0.98	0.58	0.63
TiO_2	0.00	0.05	0.00	0.00	0.00	0.00	0.00	0.03	0.00	0.00	0.00	0.01	0.00
Al_2O_3	0.28	0.39	0.40	0.18	0.54	0.64	0.17	0.01	0.05	0.04	0.08	0.14	0.11
Cr_2O_3	0.00	0.00	0.01	0.00	0.00	0.00	0.01	0.01	0.00	0.00	0.01	0.03	0.00
V_2O_3	0.00	0.01	0.00	0.00	0.00	0.01	0.01	0.00	0.02	0.00	0.02	0.00	0.02
FeO	86.69	88.89	88.87	87.86	86.97	86.25	86.86	90.86	90.50	89.68	90.57	91.73	91.34
MnO	0.66	0.37	0.54	0.83	0.75	0.73	0.96	0.54	0.70	0.33	0.32	0.37	0.23
MgO	0.03	0.03	0.06	0.10	0.07	0.11	0.20	0.02	0.03	0.02	0.02	0.00	0.02
CaO	0.24	0.29	0.08	0.09	0.34	0.60	0.19	0.00	0.01	0.00	0.00	0.00	0.00
NiO	0.01	0.00	0.00	0.00	0.00	0.00	0.00	0.00	0.00	0.00	0.00	0.00	0.00
Total	90.92	91.79	92.78	92.59	92.79	92.48	92.73	92.47	92.43	90.97	92.00	92.87	92.35

Sample	DL8#01 (wt.%)												
No.	1	2	3	4	5	6	7	8	9	11	12	13	14
SiO_2	1.14	0.93	1.29	0.90	1.36	5.18	4.94	5.25	1.87	1.62	2.02	1.18	1.23
TiO_2	0.00	0.00	0.00	0.00	0.00	0.02	0.00	0.00	0.02	0.01	0.00	0.00	0.00
Al_2O_3	0.00	0.00	0.00	0.02	0.02	0.58	0.36	0.37	0.01	0.03	0.05	0.05	0.06
Cr_2O_3	0.01	0.03	0.03	0.01	0.02	0.00	0.01	0.03	0.01	0.00	0.03	0.02	0.02
V_2O_3	0.00	0.05	0.05	0.00	0.06	0.00	0.00	0.05	0.00	0.01	0.00	0.00	0.01
FeO	91.26	91.96	90.68	90.33	91.06	86.14	87.61	87.97	90.52	90.85	91.62	91.42	92.31
MnO	0.49	0.17	0.11	0.18	0.13	0.53	0.27	0.28	0.14	0.14	0.17	0.15	0.15
MgO	0.01	0.00	0.03	0.02	0.00	0.04	0.01	0.03	0.02	0.05	0.03	0.03	0.02
CaO	0.00	0.00	0.00	0.09	0.00	0.42	0.26	0.28	0.10	0.00	0.01	0.02	0.02
NiO	0.18	0.00	0.00	0.04	0.11	0.00	0.00	0.00	0.00	0.00	0.00	0.00	0.00
Total	93.09	93.14	92.19	91.58	92.76	92.90	93.46	94.24	92.69	92.71	93.93	92.87	93.80

Sample	DL8#01				DL14-14 (wt.%)									
No.	15	16	17	18	1	2	3	4	5	6	7	8	9	11
SiO_2	5.12	4.65	3.34	5.24	0.83	0.12	0.82	4.33	1.15	0.22	3.65	2.42	4.52	0.64
TiO_2	0.00	0.01	0.00	0.00	0.00	0.00	0.00	0.05	0.00	0.00	0.00	0.00	0.00	0.00
Al_2O_3	0.46	0.33	0.11	0.37	0.00	0.01	0.03	0.00	0.00	0.02	0.00	0.02	0.00	0.00
Cr_2O_3	0.02	0.02	0.01	0.00	0.05	0.02	0.04	0.03	0.06	0.01	0.01	0.06	0.04	0.02
V_2O_3	0.00	0.04	0.00	0.02	0.00	0.00	0.00	0.00	0.00	0.11	0.00	0.00	0.00	0.01
FeO	86.69	88.68	89.82	87.84	91.68	91.32	93.31	89.77	92.42	92.65	89.74	90.44	88.19	92.37
MnO	0.58	0.64	0.47	0.64	0.22	0.16	0.40	0.36	0.48	0.18	0.28	0.17	0.38	0.17
MgO	0.01	0.07	0.00	0.04	0.11	0.00	0.03	0.17	0.00	0.00	0.08	0.02	0.15	0.01
CaO	0.20	0.09	0.00	0.19	0.00	0.00	0.00	0.22	0.01	0.08	0.13	0.33	0.33	0.05
NiO	0.00	0.00	0.00	0.01	0.29	0.18	0.04	0.00	0.00	0.00	0.00	0.00	0.00	0.00
Total	93.09	94.53	93.76	94.35	93.16	91.82	94.67	94.92	94.12	93.26	93.89	93.46	93.61	93.26

Note: Total Fe are measured and represented as FeO.

Table 2 Summary of LA-ICP-MS results for trace elements in magnetite from Baishiya deposit

Sample	DL[a]	DL15-3 (dark)						DL15-3 (light)							
No.		1	SD	2	SD	3	SD	1	SD	2	SD	3	SD	4	SD
Si	197	8175	189	7003	214	5150	221	2032	167	1667	116	1917	138	1263	120
Mg	4.77	3652	49.2	2474	47.2	2671	43.5	1508	25.9	1548	24.9	1660	31.0	1346	29.1
Al	1.94	8791	92.6	6745	102	6803	68.0	1992	17.2	1427	15.2	2034	25.5	1540	19.9
Ca	82.3	3166	108	2868	90.6	1868	88.9	115	49.8	108	50.6	175	45.7	92.2	51.6
Sc	0.131	0.422	0.134	0.369	0.145	0.177	0.141	0.690	0.162	0.400	0.152	0.215	0.188	0.368	0.126
Ti	0.355	51.2	6.75	116	7.68	14.2	3.06	576	20.7	292	14.5	1475	36.2	552	24.0
V	0.127	1.45	0.249	7.19	0.552	0.82	0.218	19.1	1.24	6.20	0.509	49.2	1.64	20.0	1.16
Cr	1.15	b.d.l.		3.00	1.28	b.d.l.		b.d.l.		6.53	7.80	4.92	1.33	b.d.l.	
Mn	1.01	1287	15.3	1163	16.2	1909	26.3	1456	12.9	578	5.40	1463	17.4	1344	17.4
Co	0.127	7.98	0.489	9.86	0.629	3.69	0.484	4.19	0.431	4.41	0.482	4.74	0.660	4.00	0.402
Ni	0.25	0.261	0.237	0.551	0.506	1.50	0.669	4.61	1.81	9.58	1.40	1.97	0.608	0.368	0.447
Cu	1.15	b.d.l.		b.d.l.		2.31	1.00	1.25	1.24	b.d.l.		b.d.l.		1.48	0.776
Zn	0.508	294	9.17	223	7.49	336	10.0	190	7.03	87.1	6.23	211	8.20	151	7.04
Ga	0.081	17.9	1.08	15.8	0.985	15.7	0.966	11.5	0.932	9.86	0.855	14.8	0.847	10.4	0.757
Ge	0.221	2.07	0.419	1.65	0.361	1.91	0.330	2.12	0.392	1.40	0.324	1.75	0.318	1.52	0.292
Rb	0.128	1.36	0.272	0.868	0.200	2.12	1.07	0.962	0.232	1.75	0.909	0.754	0.299	0.160	0.106
Sr	0.001	17.3	0.743	11.4	0.581	11.8	0.590	1.50	0.345	1.89	1.30	1.35	0.189	0.360	0.089
Y	0.001	0.514	0.099	0.235	0.081	1.52	0.198	0.554	0.125	0.129	0.058	0.280	0.073	0.124	0.057
Zr	0.002	5.82	0.522	2.79	0.330	5.47	0.483	1.29	0.227	0.361	0.105	1.17	0.216	0.390	0.124
Nb	0.001	11.4	0.584	5.64	0.394	8.46	0.806	0.245	0.088	1.43	0.531	0.748	0.127	0.333	0.086
Mo	0.001	0.147	0.147	0.206	0.118	0.302	0.184	1.55	0.528	2.26	0.732	0.615	0.259	0.364	0.262
Ag	0.003	0.537	0.434	0.644	0.494	0.047	0.035	0.294	0.092	0.328	0.108	0.157	0.061	0.061	0.043
Cd	0.009	0.068	0.068	0.064	0.064	0.071	0.071	0.452	0.294	0.637	0.260	0.191	0.142	0.822	0.579
In	0.019	1.34	0.149	0.621	0.079	0.841	0.107	0.904	0.343	0.911	0.259	0.687	0.096	0.364	0.068
Sn	0.265	16.2	1.07	11.6	1.07	10.8	1.05	5.23	0.587	4.55	0.544	6.28	0.705	4.77	0.725
Ba	0.051	10.5	1.03	5.48	0.749	4.48	0.716	3.40	1.68	0.537	0.297	1.23	0.387	0.838	0.324
Hf	0.001	0.124	0.029	0.053	0.019	0.184	0.089	0.279	0.045	0.142	0.032	0.120	0.031	0.097	0.029
Ta	0.001	0.422	0.045	0.449	0.042	0.485	0.046	0.445	0.043	0.379	0.050	0.206	0.041	0.131	0.024
W	0.004	1.45	0.310	1.12	0.201	0.326	0.077	0.839	0.238	1.12	0.308	0.422	0.110	0.162	0.063
Pb	0.008	0.514	0.075	0.374	0.075	0.516	0.101	0.414	0.246	1.01	0.353	0.38	0.062	0.11	0.032
Bi	0.009	0.426	0.168	0.228	0.088	0.264	0.084	0.906	0.398	0.686	0.198	1.83	1.49	0.108	0.042
Th	0.001	0.194	0.031	0.153	0.021	0.113	0.018	0.268	0.036	0.321	0.077	0.202	0.064	0.046	0.013
U	0.001	0.692	0.159	0.504	0.124	0.629	0.246	0.741	0.143	1.02	0.244	0.242	0.049	0.211	0.066
Nb/Ta		27.00		12.59		17.43		0.55		3.78		3.63		2.55	
Zr/Hf		46.82		52.64		29.70		4.61		2.54		9.76		4.03	

Sample	DL15-3 (light)										DL2#01 (dark)			
No.	5	SD	6	SD	7	SD	8	SD	9	SD	1	SD	2	SD
Si	1444	112	1008	131	1644	220	923	130	701	114	16005	238	14624	267
Mg	3465	47.8	1961	38.0	3473	52.3	3444	52.1	3387	49.1	357	12.2	775	17.7
Al	1042	12.7	642	9.20	489	12.0	759	12.1	1003	10.5	2308	29.2	997	14.8
Ca	88.2	48.4	184	49.5	101	48.8	b.d.l.		166	51.6	2577	87.3	1716	66.5
Sc	0.137	0.138	0.294	0.118	0.295	0.133	0.143	0.099	0.384	0.157	0.674	0.154	0.198	0.14
Ti	736	26.0	110	8.02	870	30.0	275	14.0	600	19.8	2.45	1.49	8.31	3.44
V	28.6	1.02	3.98	0.791	41.6	1.43	7.37	0.741	10.1	0.613	0.14	0.094	2.93	0.360
Cr	5.06	1.74	b.d.l.		3.47	1.36	b.d.l.		b.d.l.		b.d.l.		b.d.l.	
Mn	2183	21.4	1291	14.4	1465	19.4	1764	25.4	1995	27.0	3613	28.5	5854	87.2
Co	1.96	0.290	3.97	0.377	9.35	0.821	6.11	0.488	5.30	0.711	3.48	0.388	4.87	0.407
Ni	4.61	1.02	3.56	0.841	29.0	2.48	2.71	0.825	2.77	0.761	1.37	0.443	1.07	0.529
Cu	b.d.l.		1.16	0.900	4.62	2.78	3.13	0.858	b.d.l.		2.31	0.749	26.2	26.8
Zn	321	9.28	162	5.29	264	8.25	252	8.78	294	10.0	231	7.19	231	8.33
Ga	9.87	0.763	10.1	0.957	13.3	1.04	7.82	0.705	11.6	0.886	7.99	0.582	6.69	0.639
Ge	0.76	0.264	1.91	0.654	3.75	1.37	1.77	0.404	0.96	0.285	2.98	0.463	3.63	0.484
Rb	0.210	0.089	1.93	0.684	1.09	0.328	0.667	0.256	0.156	0.079	0.378	0.129	0.734	0.146
Sr	0.513	0.143	0.300	0.103	1.17	0.458	0.240	0.120	b.d.l.		2.77	0.255	3.56	0.274
Y	0.076	0.039	0.167	0.057	0.093	0.039	0.062	0.037	0.053	0.042	b.d.l.		0.082	0.035
Zr	0.643	0.141	0.654	0.174	0.497	0.166	0.598	0.158	0.485	0.135	0.430	0.124	0.186	0.079
Nb	0.443	0.130	0.622	0.143	2.16	0.630	0.801	0.218	0.268	0.101	0.230	0.089	0.228	0.079
Mo	0.297	0.209	2.21	1.50	2.11	0.910	0.344	0.180	0.284	0.173	0.195	0.145	0.314	0.226
Ag	0.077	0.046	0.360	0.156	0.509	0.173	0.503	0.254	0.060	0.036	0.013	0.013	0.428	0.122
Cd	0.212	0.212	b.d.l.		0.308	0.161	0.255	0.155	0.194	0.144	b.d.l.		b.d.l.	
In	1.07	0.638	0.497	0.119	0.762	0.170	0.703	0.261	0.395	0.060	0.179	0.037	0.312	0.058
Sn	11.8	0.992	13.4	1.34	8.21	0.871	6.16	0.779	5.97	0.667	25.9	1.30	23.0	1.41
Ba	0.154	0.154	0.571	0.263	1.77	0.705	0.571	0.282	0.074	0.074	2.88	0.540	2.48	0.568
Hf	0.129	0.035	0.200	0.042	0.085	0.022	0.060	0.019	0.090	0.035	0.023	0.019	0.005	0.005
Ta	0.187	0.044	0.405	0.132	0.381	0.104	0.155	0.026	0.166	0.029	0.027	0.017	0.009	0.008
W	0.512	0.240	1.50	0.631	0.676	0.162	0.346	0.131	0.086	0.042	10.8	0.382	27.6	0.931
Pb	1.55	0.129	2.26	1.32	0.875	0.279	0.291	0.083	0.064	0.029	3.17	0.175	44.8	7.62
Bi	0.156	0.069	0.262	0.065	1.56	0.938	0.30	0.097	0.075	0.043	0.052	0.041	0.546	0.107
Th	0.076	0.015	0.366	0.156	0.184	0.032	0.114	0.022	0.054	0.015	0.005	0.004	0.049	0.011
U	0.190	0.054	1.18	0.342	1.35	0.344	0.636	0.187	0.120	0.026	0.164	0.042	1.34	0.063
Nb/Ta	2.36		1.54		5.66		5.16		1.62		8.52		24.03	
Zr/Hf	4.98		3.27		5.86		9.99		5.36		18.39		38.66	

Sample	DL2#01 (light)				DL8#01									
No.	1	SD	2	SD	1	SD	2	SD	3	SD	4	SD	5	SD

Si	3754	133	4621	152	20444	770	21339	592	17723	486	28747	555	17294	461
Mg	130	7.05	45.3	3.94	604	31.4	370	19.7	236	16.4	362	14.5	448	21.5
Al	789	7.70	763	16.0	1283	41.6	1289	47.1	937	35.9	2320	44.6	910	21.1
Ca	988	56.7	743	61.5	2438	124	1412	102	1310	88.8	2304	102	3265	145
Sc	0.486	0.151	0.489	0.123	2.18	0.481	1.52	0.330	1.02	0.235	1.14	0.247	0.622	0.183
Ti	21.7	4.32	105.8	11.7	25.1	8.66	19.2	5.89	8.87	3.82	9.44	3.54	14.1	3.73
V	5.89	0.456	8.40	0.635	29.0	2.75	14.7	1.28	13.7	1.07	4.53	0.568	8.77	0.629
Cr	1.85	1.29	b.d.l.		3.19	1.92	3.04	1.76	4.08	1.66	6.50	1.80	3.35	1.51
Mn	3630	31.2	2947	20.2	4193	246	2389	57.1	1849	37.2	2865	56.0	4899	160.6
Co	2.46	0.293	2.57	0.274	33.3	1.45	33.1	1.51	33.6	1.30	30.5	1.14	36.9	1.26
Ni	15.0	1.52	2.51	0.758	16.5	2.08	13.4	4.40	6.80	1.40	5.91	1.24	9.18	1.54
Cu	b.d.l.		b.d.l.		12.6	2.77	6.10	1.55	3.33	1.33	4.39	3.03	2.62	1.05
Zn	200	6.11	152	4.87	310	10.5	335	10.9	370	11.3	502	12.1	580	16.0
Ga	7.56	0.651	10.8	0.608	21.4	1.73	16.5	1.24	14.7	1.58	11.0	0.907	9.55	0.959
Ge	0.65	0.176	4.17	0.540	16.7	1.42	13.6	1.27	14.8	1.18	19.8	1.28	16.0	1.20
Rb	0.205	0.124	b.d.l.	0.080	5.93	0.964	4.69	0.972	2.73	0.534	2.83	0.394	1.97	0.413
Sr	0.952	0.128	0.763	0.124	13.5	1.06	7.45	0.600	5.75	0.459	8.16	0.562	10.2	0.575
Y	0.034	0.026	b.d.l.		1.55	0.195	0.779	0.143	1.08	0.176	0.707	0.125	0.642	0.167
Zr	0.815	0.660	0.169	0.065	1.22	0.270	0.914	0.259	1.60	0.655	0.780	0.206	0.502	0.160
Nb	0.045	0.033	0.028	0.013	3.80	0.452	3.12	1.79	1.99	0.388	1.23	0.213	0.873	0.240
Mo	0.248	0.195	b.d.l.		17.4	4.33	3.83	0.761	3.51	0.859	6.50	2.70	3.37	0.662
Ag	0.025	0.025	0.024	0.024	3.50	0.606	1.45	0.322	1.11	0.247	0.775	0.160	0.835	0.211
Cd	0.120	0.085	b.d.l.		3.56	0.820	1.84	0.510	0.470	0.331	0.461	0.214	0.993	0.319
In	b.d.l.		b.d.l.		6.83	1.78	2.22	0.479	1.54	0.217	1.43	0.192	1.14	0.362
Sn	4.81	0.970	9.68	0.871	28.8	6.18	12.9	1.14	16.2	1.43	8.06	1.17	6.80	1.43
Ba	0.128	0.128	0.365	0.190	7.81	1.69	8.56	1.59	9.81	1.43	20.3	1.64	6.16	0.974
Hf	0.098	0.070	0.010	0.009	0.536	0.077	0.274	0.058	0.312	0.067	0.206	0.043	0.224	0.052
Ta	0.019	0.016	0.011	0.010	1.65	0.215	1.06	0.267	1.06	0.258	0.446	0.069	0.462	0.085
W	0.638	0.119	0.546	0.081	170	11.8	70.1	2.43	114	5.01	31.6	2.37	36.4	3.51
Pb	0.477	0.079	1.65	0.164	30.6	2.04	15.4	0.977	24.8	1.21	13.4	0.725	10.1	0.564
Bi	0.034	0.013	b.d.l.		4.16	0.648	1.79	0.325	2.73	0.516	1.44	0.395	0.942	0.140
Th	0.233	0.025	0.026	0.011	1.58	0.250	0.450	0.046	0.509	0.063	0.493	0.180	0.274	0.033
U	0.122	0.031	0.089	0.038	13.4	1.29	5.29	0.283	2.69	0.239	2.68	0.301	2.72	0.202
Nb/Ta	2.37		2.49		2.30		2.94		1.87		2.76		1.89	
Zr/Hf	8.33		16.91		2.27		3.34		5.15		3.79		2.24	

Sample	DL8#01													
No.	6	SD	7	SD	8	SD	9	SD	10	SD	11	SD	12	SD
Si	16924	451	12913	334	28605	1079	15309	447	12151	362	25292	371	11238	529
Mg	185	11.9	744	34.2	818	36.8	285	19.8	192	16.8	503	22.2	105	9.18

Al	917	26.8	498	12.6	1482	42.8	587	20.2	521	12.3	2313	25.4	418	13.8
Ca	1381	89.2	4274	203	3041	127	1125	87.8	1140	68.8	3540	113	601	110
Sc	1.02	0.180	0.932	0.238	3.20	0.581	1.44	0.263	0.814	0.235	0.715	0.221	1.11	0.258
Ti	21.1	5.50	26.2	4.93	37.1	6.95	29.5	4.44	17.0	3.63	21.2	9.10	10.1	3.39
V	14.7	1.00	23.5	1.12	29.9	1.96	30.7	1.36	15.3	0.899	5.82	0.620	16.4	1.25
Cr	b.d.l.		b.d.l.		21.22	7.57	b.d.l.		1.93	1.49	b.d.l.		b.d.l.	
Mn	1633	27.7	6769	259	3314	40.8	1574	26.9	1176	19.2	4184	86.5	1258	42.9
Co	29.1	1.10	32.9	1.20	43.9	1.86	33.1	1.47	28.4	1.35	33.9	1.17	28.8	1.54
Ni	2.69	0.943	8.40	1.54	24.1	2.44	14.6	2.06	5.59	1.17	7.24	1.33	6.71	1.39
Cu	3.60	1.01	5.98	1.27	9.50	1.81	b.d.l.		b.d.l.	1.30	b.d.l.		4.32	1.04
Zn	332	18.5	328	11.9	327	13.4	198	8.43	154	6.36	291	9.64	182	9.24
Ga	11.2	0.945	10.2	1.10	27.2	2.49	12.1	0.991	12.1	1.24	12.3	0.984	10.0	0.939
Ge	15.8	1.19	8.45	0.947	25.2	2.91	13.3	0.991	11.6	1.45	16.4	1.20	10.1	1.03
Rb	2.20	0.378	1.39	0.282	10.4	1.32	4.91	0.632	2.31	0.323	2.24	0.422	1.07	0.240
Sr	5.94	0.495	13.7	0.651	10.7	0.687	7.82	0.478	7.26	0.475	13.0	0.713	3.12	0.408
Y	1.21	0.194	0.664	0.129	2.14	0.272	1.66	0.226	1.27	0.179	0.623	0.121	0.711	0.145
Zr	0.685	0.216	1.13	0.275	2.30	0.375	2.45	1.05	0.805	0.180	0.499	0.145	0.593	0.254
Nb	0.782	0.204	0.614	0.222	5.58	0.541	2.68	0.400	1.61	0.399	1.48	0.339	0.879	0.217
Mo	4.85	0.874	5.99	0.972	12.6	1.71	10.7	1.36	7.36	0.950	3.07	0.650	3.90	0.939
Ag	0.469	0.127	0.197	0.076	2.71	0.404	1.53	0.526	0.620	0.148	0.434	0.132	0.389	0.139
Cd	0.467	0.289	0.745	0.393	4.50	1.14	1.05	0.441	0.720	0.262	0.940	0.381	1.19	0.446
In	1.00	0.395	0.818	0.182	6.24	0.934	2.47	0.289	0.969	0.141	1.86	0.559	0.615	0.123
Sn	16.8	1.55	14.9	1.32	32.1	4.91	25.5	2.73	23.8	1.46	8.27	0.861	18.2	1.55
Ba	7.92	1.25	4.12	0.792	14.9	1.69	6.55	0.983	5.90	0.938	20.3	1.85	2.98	0.703
Hf	0.165	0.041	0.160	0.044	1.34	0.127	0.527	0.103	0.287	0.052	0.288	0.055	0.186	0.052
Ta	0.417	0.071	0.327	0.065	3.52	0.375	0.988	0.100	0.481	0.062	0.539	0.070	0.188	0.043
W	161	5.86	219	8.17	78.0	3.30	182	2.92	175	2.50	31.9	1.37	146	6.68
Pb	27.8	1.19	25.0	1.06	33.0	1.38	48.1	1.25	53.5	0.893	25.0	0.596	29.3	1.34
Bi	0.959	0.243	0.695	0.149	5.88	0.799	2.27	0.256	1.61	0.237	0.721	0.112	0.937	0.202
Th	0.193	0.034	0.533	0.172	1.97	0.120	0.748	0.061	0.448	0.070	0.410	0.052	0.233	0.053
U	2.43	0.165	4.43	0.186	11.3	0.840	5.87	0.371	3.97	0.246	2.23	0.244	2.56	0.187
Nb/Ta	1.87		1.88		1.58		2.71		3.35		2.75		4.66	
Zr/Hf	4.14		7.05		1.72		4.64		2.81		1.73		3.19	

Sample	DL8#01						DL14-14							
No.	13	SD	14	SD	15	SD	1	SD	2	SD	3	SD	4	SD
Si	27893	956	14462	433	19753	360	2615	142	4503	162	5153	161	6062	211
Mg	365	15.4	190	10.5	207	10.6	3049	47.1	593	18.1	1322	26.2	1156	23.2
Al	1734	23.4	736	15.9	1062	25.6	53.5	2.93	46.8	3.17	49.9	3.11	57.3	2.55
Ca	2752	102	1401	68.6	1006	64.0	178	49.5	275	50.1	96.8	49.4	194	43.7

Sc	1.70	0.326	0.489	0.163	1.34	0.233	0.243	0.107	0.363	0.105	0.362	0.101	0.363	0.138
Ti	17.8	4.66	14.2	3.21	16.2	7.37	3.08	1.68	4.29	0.946	3.86	1.51	16.0	3.51
V	13.9	1.30	17.0	0.854	6.24	1.05	1.81	0.359	0.56	0.213	2.10	0.311	5.23	1.12
Cr	8.76	2.66	5.83	1.77	1.86	1.29	b.d.l.		b.d.l.		b.d.l.		3.05	1.24
Mn	3894	80.1	1751	28.3	2065	28.1	2755	29.3	2878	30.0	2778	25.5	3077	26.3
Co	40.7	2.05	28.8	1.12	32.2	1.28	1.09	0.194	7.76	0.588	7.49	0.541	7.89	0.507
Ni	13.2	2.17	13.1	3.73	4.10	1.41	3.19	0.683	3.97	0.967	3.03	0.951	3.42	0.674
Cu	12.4	1.78	3.65	0.744	3.37	1.07	b.d.l.		b.d.l.		b.d.l.		b.d.l.	
Zn	314	8.77	160	5.61	210	6.48	192	7.18	141	5.84	165	6.05	174	5.25
Ga	21.2	1.88	9.65	0.841	10.0	0.789	1.05	0.625	2.83	0.370	1.47	0.301	2.25	0.302
Ge	17.6	1.56	12.2	1.23	16.9	1.18	2.18	0.499	2.27	0.433	1.43	0.284	1.90	0.356
Rb	10.5	1.48	2.29	0.303	2.78	0.482	b.d.l.		0.326	0.140	0.255	0.102	0.275	0.183
Sr	12.2	0.704	5.99	0.441	3.83	0.320	0.221	0.084	0.429	0.108	0.526	0.142	0.348	0.111
Y	2.41	0.276	1.23	0.134	0.670	0.128	1.11	0.147	2.19	0.234	2.88	0.289	3.32	0.268
Zr	2.12	0.336	1.52	0.249	0.479	0.143	0.865	0.181	1.88	0.295	4.26	0.435	5.08	0.458
Nb	4.16	0.485	1.12	0.194	0.824	0.147	0.580	0.352	0.231	0.139	0.146	0.077	0.298	0.192
Mo	12.3	2.30	5.06	1.17	2.07	0.595	0.360	0.237	1.39	0.824	0.547	0.252	0.442	0.186
Ag	2.84	0.368	1.21	0.245	0.723	0.199	0.396	0.234	0.089	0.051	0.102	0.078	0.027	0.019
Cd	4.38	0.794	1.11	0.415	1.10	0.374	b.d.l.		0.128	0.090	0.063	0.063	b.d.l.	
In	7.91	1.17	1.75	0.227	1.38	0.227	0.394	0.070	1.57	0.757	0.120	0.032	0.164	0.081
Sn	16.8	1.89	20.1	1.95	4.17	0.612	6.74	0.932	8.46	0.871	9.48	0.791	11.4	0.912
Ba	12.5	1.31	8.10	0.942	9.85	1.47	0.151	0.106	0.365	0.217	0.500	0.254	0.132	0.132
Hf	1.58	0.147	0.761	0.140	0.299	0.049	0.099	0.032	0.042	0.016	0.051	0.017	0.053	0.021
Ta	2.60	0.203	0.900	0.111	0.682	0.081	0.108	0.024	0.045	0.016	0.072	0.021	0.026	0.014
W	42.7	2.18	92.2	2.25	10.2	0.606	2.87	0.257	5.17	0.302	7.27	0.296	8.09	0.393
Pb	16.2	0.979	25.3	0.671	6.83	0.405	2.51	1.19	0.857	0.093	1.123	0.139	1.84	0.501
Bi	5.60	0.594	1.30	0.172	1.28	0.200	0.174	0.090	0.369	0.160	0.023	0.014	0.113	0.049
Th	2.15	0.152	0.712	0.058	0.513	0.062	0.105	0.020	0.043	0.014	0.025	0.008	0.039	0.012
U	13.3	1.12	3.37	0.254	2.69	0.230	1.97	1.27	0.437	0.079	0.603	0.150	0.779	0.263
Nb/Ta	1.60		1.24		1.21		5.38		5.13		2.03		11.65	
Zr/Hf	1.35		2.00		1.60		8.77		44.62		82.76		96.63	

DL, detection limit; SD, standard deviation; b.d.l., below detection limit.

[a] DL=3×$\sigma^{i}_{\text{background}}$×$C^{i}_{RM}$ /cps^{i}_{RM}, where $\sigma^{i}_{\text{background}}$ is the standard deviation of multiple determinations of element *i* in the background and C^{i}_{RM} and cps^{i}_{RM} are the concentration and peak intensity of element *i* in the reference material, respectively

Figure 1

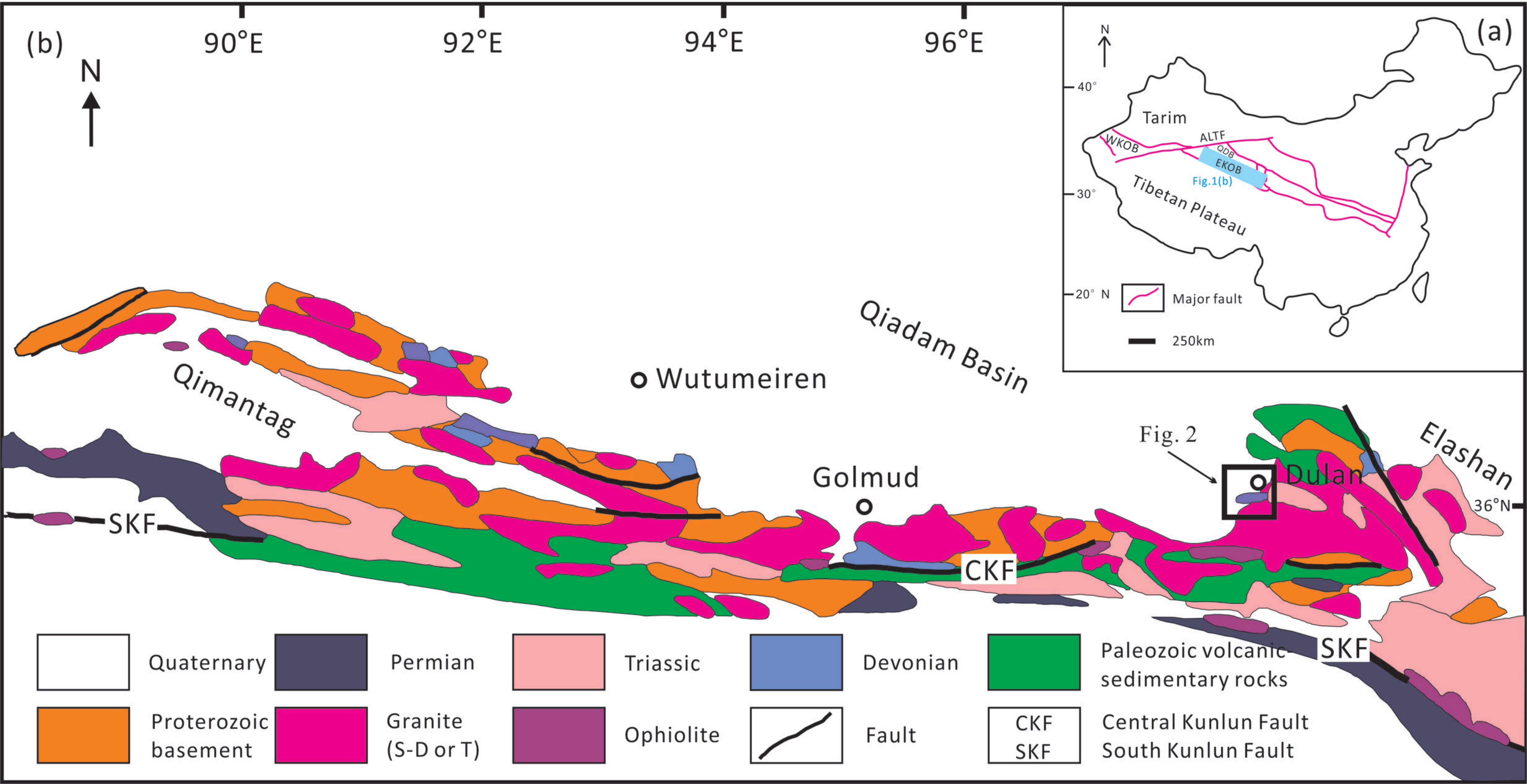
(b)
90°E
92°E
94°E
96°E
N
36°N
Qimantag
Wutumeiren
Qiadam Basin
Golmud
Fig. 2
Dulan
Elashan
SKF
CKF
SKF
Quaternary
Permian
Triassic
Devonian
Paleozoic volcanic-sedimentary rocks
Proterozoic basement
Granite (S-D or T)
Ophiolite
Fault
CKF SKF
Central Kunlun Fault
South Kunlun Fault
(a)
N
40°
30°
20° N
Tarim
ALTF
WKOB
QDB
EKOB
Fig.1(b)
Tibetan Plateau
Major fault
250km

Figure 2

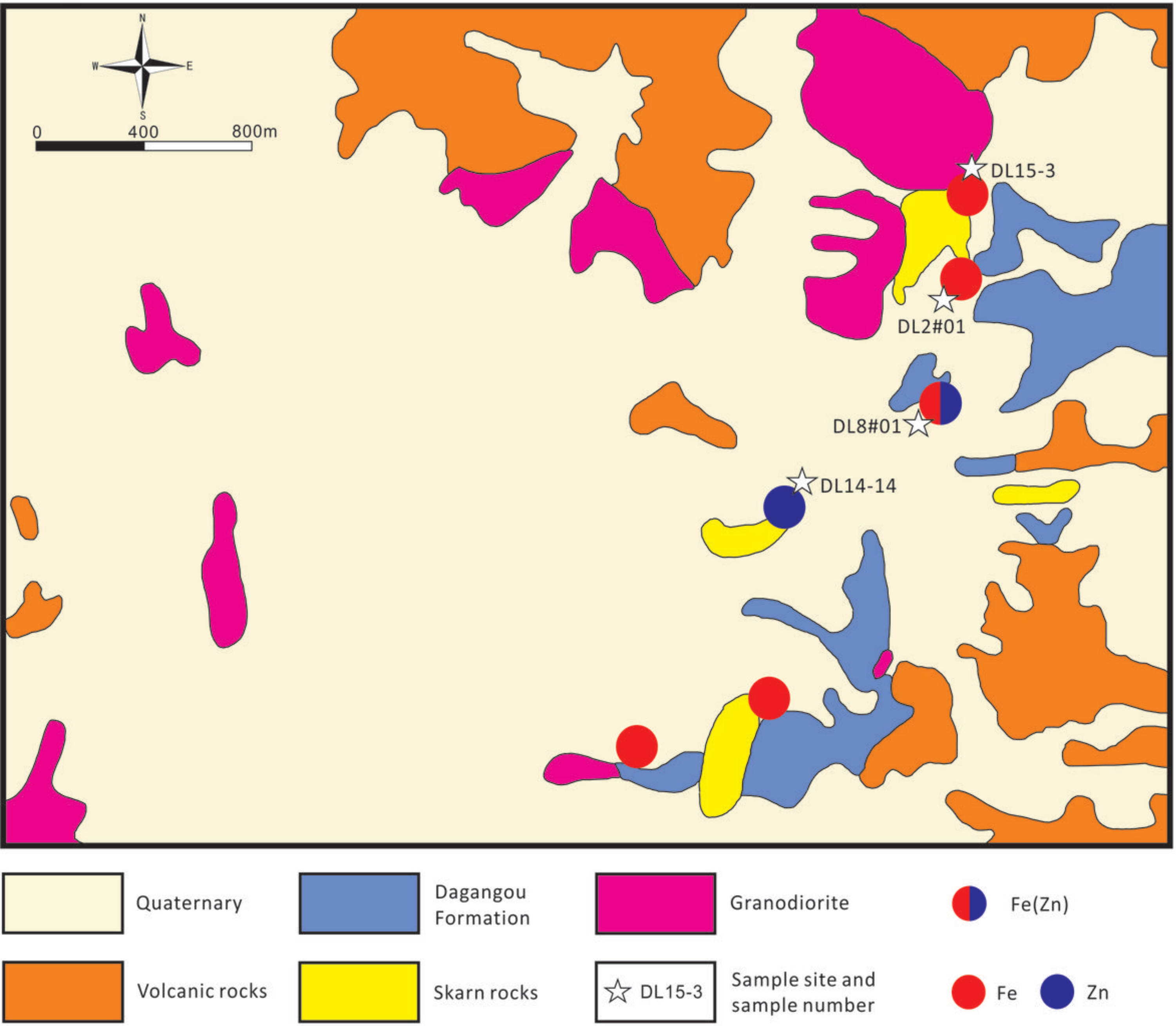
N
W
E
S
0
400
800m
DL15-3
DL2#01
DL8#01
DL14-14
Quaternary
Dagangou Formation
Granodiorite
Fe(Zn)
Volcanic rocks
Skarn rocks
☆ DL15-3
Sample site and sample number
Fe
Zn

Figure 3

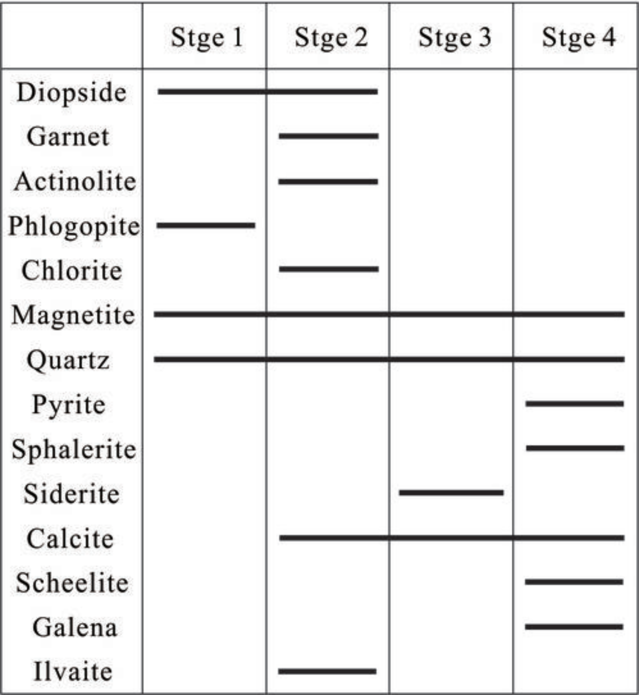
Stge 1
Stge 2
Stge 3
Stge 4
Diopside
Garnet
Actinolite
Phlogopite
Chlorite
Magnetite
Quartz
Pyrite
Sphalerite
Siderite
Calcite
Scheelite
Galena
Ilvaite

Figure 4

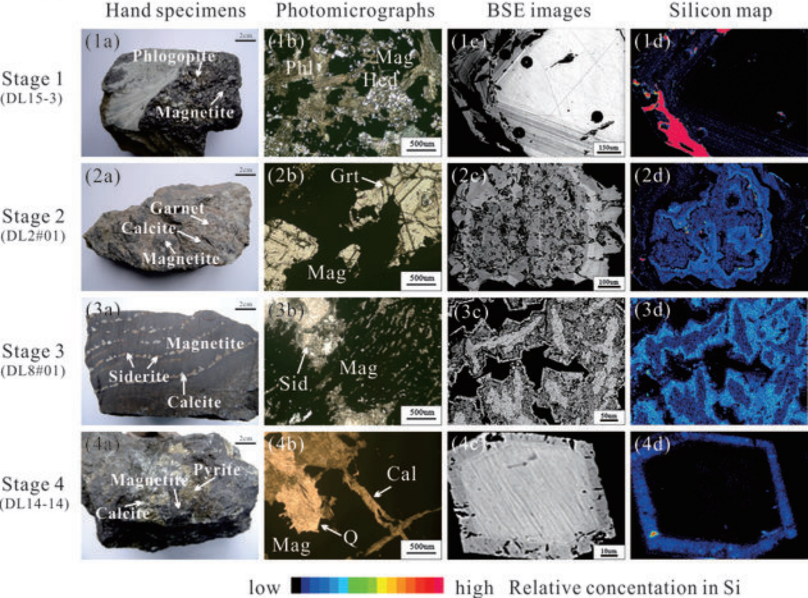
Hand specimens
Photomicrographs
BSE images
Silicon map
Stage 1
(DL15-3)
(1a)
2cm
Phlogopite
Magnetite
(1b)
Phl
Mag
Hed
500um
(1c)
150um
(1d)
Stage 2
(DL2#01)
(2a)
2cm
Garnet
Calcite
Magnetite
(2b)
Grt
Mag
500um
(2c)
100um
(2d)
Stage 3
(DL8#01)
(3a)
2cm
Magnetite
Siderite
Calcite
(3b)
Sid
Mag
500um
(3c)
50um
(3d)
Stage 4
(DL14-14)
(4a)
2cm
Magnetite
Pyrite
Calcite
(4b)
Cal
Mag
Q
500um
(4c)
10um
(4d)
low
high
Relative concentation in Si

Figure 5

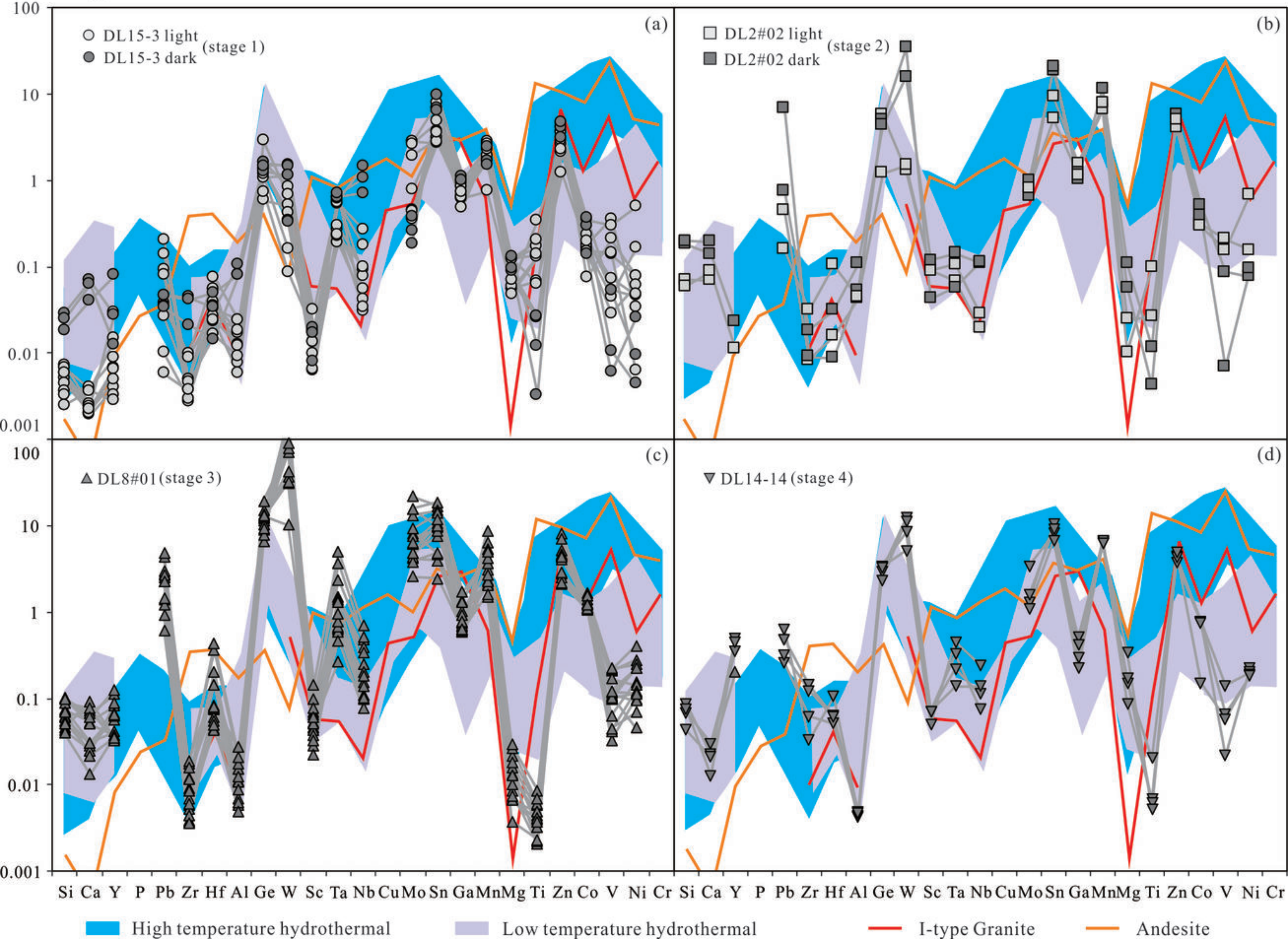
(a)
DL15-3 light
DL15-3 dark
(stage 1)
(b)
DL2#02 light
DL2#02 dark
(stage 2)
(c)
DL8#01 (stage 3)
(d)
DL14-14 (stage 4)
100
10
1
0.1
0.01
0.001
Si Ca Y P Pb Zr Hf Al Ge W Sc Ta Nb Cu Mo Sn Ga Mn Mg Ti Zn Co V Ni Cr
High temperature hydrothermal
Low temperature hydrothermal
I-type Granite
Andesite

Figure 6

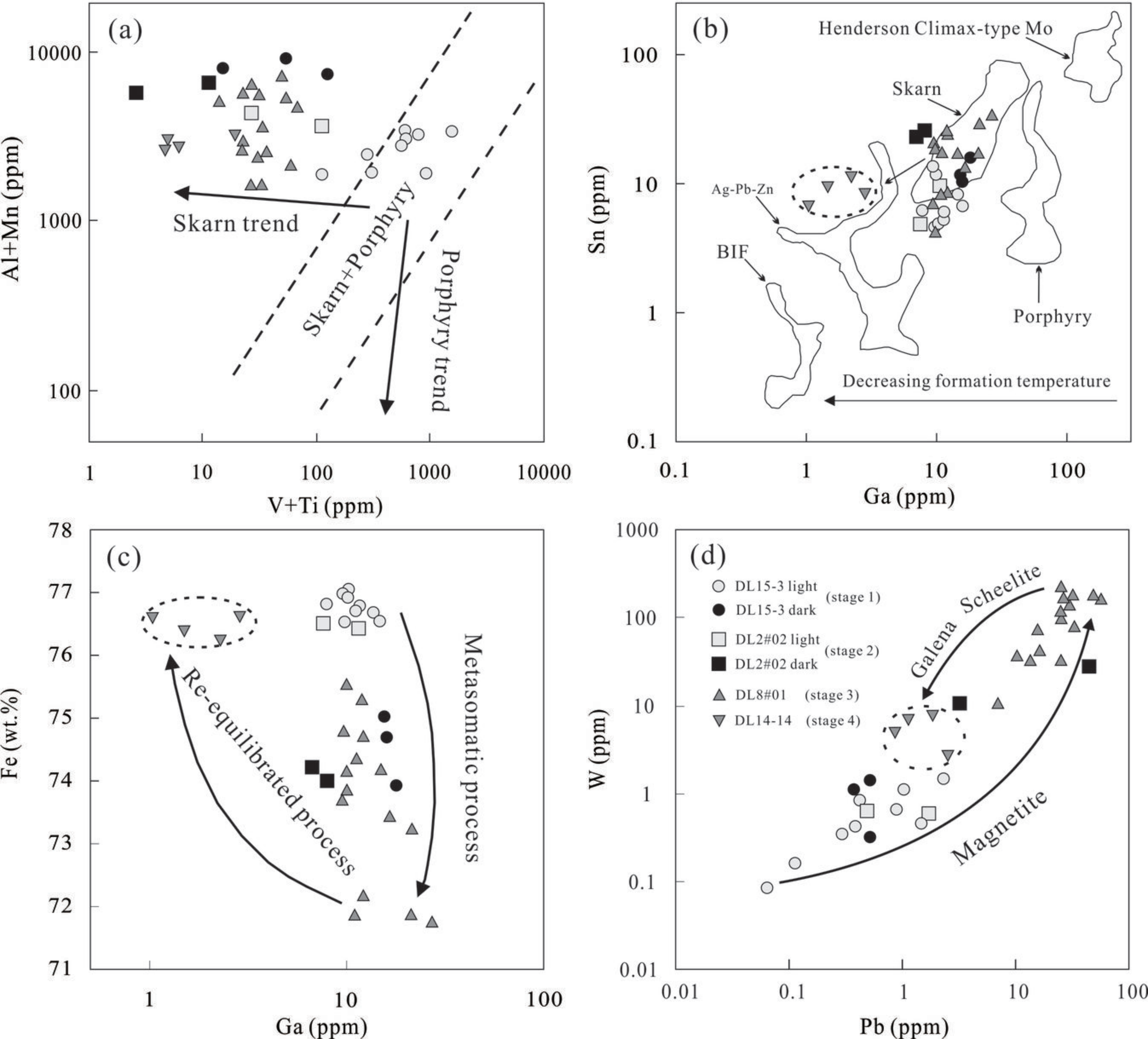
(a)
Al+Mn (ppm)
10000
1000
100
V+Ti (ppm)
1
10
100
1000
10000
Skarn trend
Skarn+Porphyry
Porphyry trend
(b)
Henderson Climax-type Mo
Skarn
Ag-Pb-Zn
BIF
Porphyry
Decreasing formation temperature
Sn (ppm)
100
10
1
0.1
Ga (ppm)
0.1
1
10
100
(c)
Fe (wt.%)
78
77
76
75
74
73
72
71
Ga (ppm)
1
10
100
Re-equilibrated process
Metasomatic process
(d)
DL15-3 light
DL15-3 dark
(stage 1)
DL2#02 light
DL2#02 dark
(stage 2)
DL8#01 (stage 3)
DL14-14 (stage 4)
Galena
Scheelite
Magnetite
W (ppm)
1000
100
10
1
0.1
0.01
Pb (ppm)
0.01
0.1
1
10
100

Figure 7

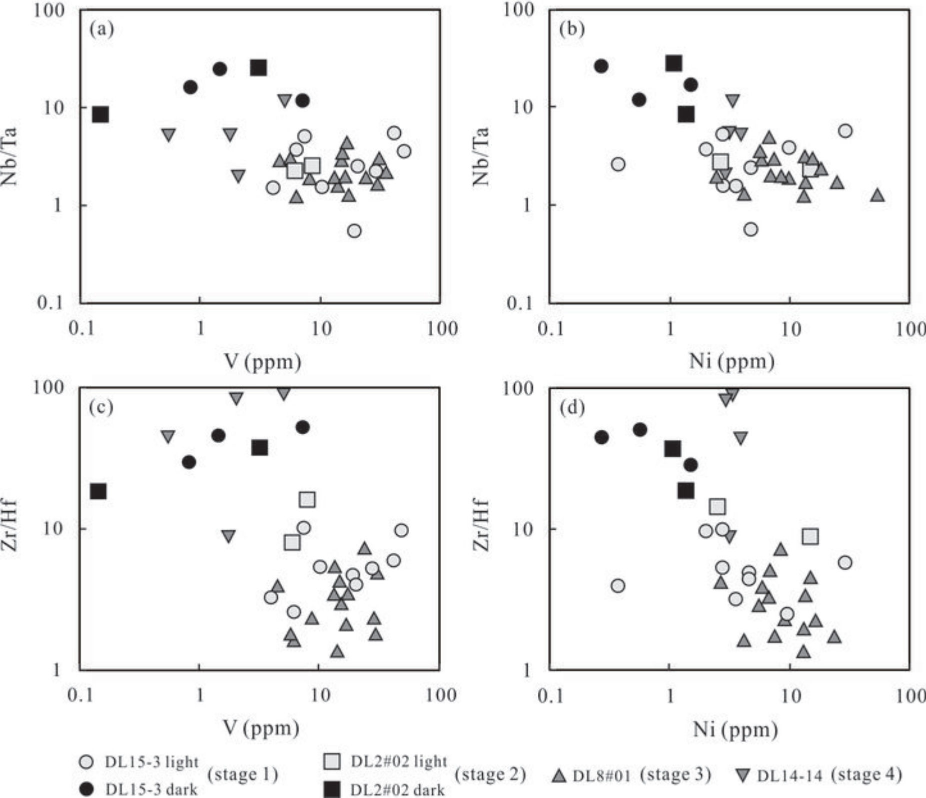
(a)
(b)
(c)
(d)
Nb/Ta
Zr/Hf
V (ppm)
Ni (ppm)
100
10
1
0.1
0.1
1
10
100
DL15-3 light
DL15-3 dark
(stage 1)
DL2#02 light
DL2#02 dark
(stage 2)
DL8#01 (stage 3)
DL14-14 (stage 4)

Figure 8

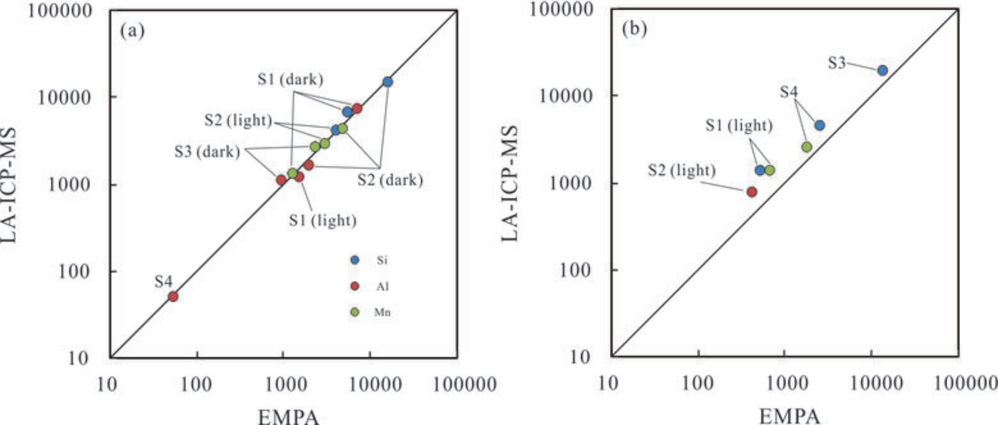
(a)
(b)
LA-ICP-MS
EMPA
10
100
1000
10000
100000
S1 (dark)
S2 (light)
S3 (dark)
S2 (dark)
S1 (light)
S4
Si
Al
Mn
S3
S4
S1 (light)
S2 (light)

Figure 9

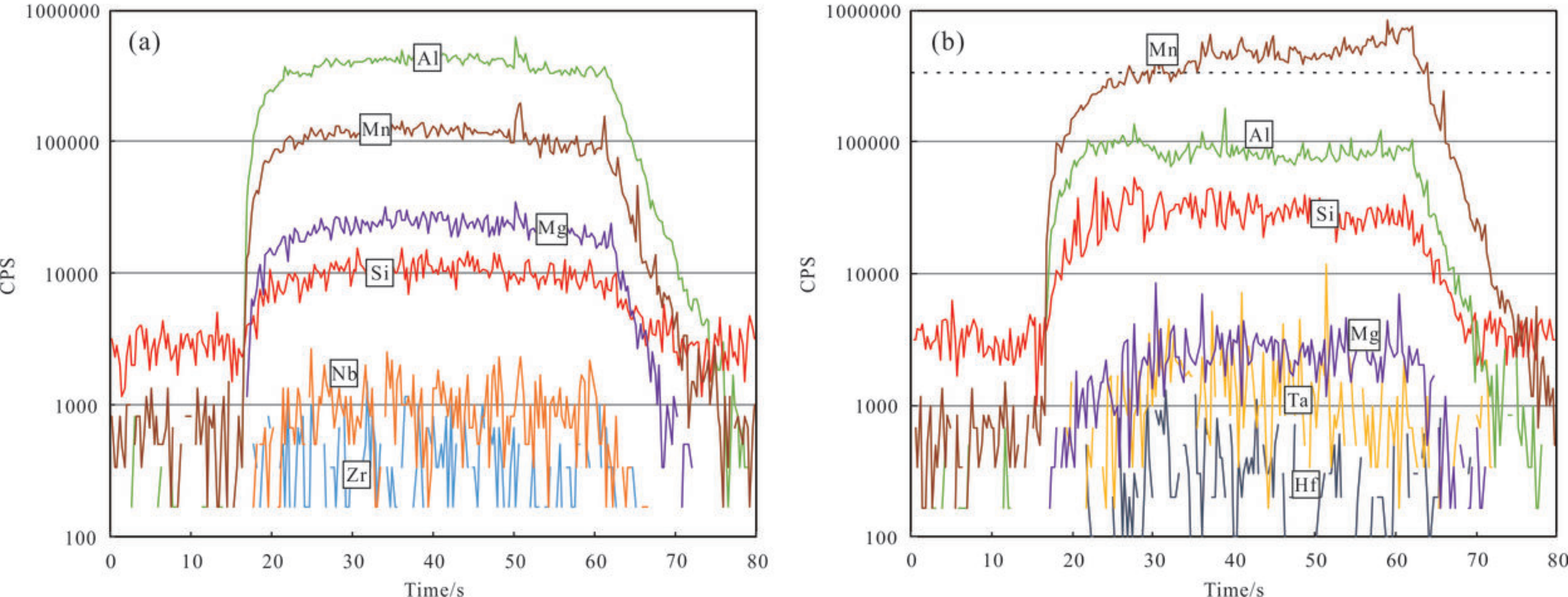
(a)
1000000
100000
10000
1000
100
CPS
Al
Mn
Mg
Si
Nb
Zr
0
10
20
30
40
50
60
70
80
Time/s
(b)
1000000
100000
10000
1000
100
CPS
Mn
Al
Si
Mg
Ta
Hf
0
10
20
30
40
50
60
70
80
Time/s

Figure 10